Rad54B serves as a scaffold in the DNA damage response that limits checkpoint strength

Takaaki Yasuhara[1], Takahiko Suzuki[2], Mari Katsura[3], and Kiyoshi Miyagawa[1,*]

[1]Laboratory of Molecular Radiology, Center for Disease Biology and Integrative Medicine, Graduate School of Medicine, The University of Tokyo, 7-3-1 Hongo, Bunkyo-ku, Tokyo, Japan

[2]Department of Radiological Technology, Faculty of Medical Technology, Teikyo University, 2-11-1 Kaga, Itabashi-ku, Tokyo, Japan

[3]Radioisotope Center, The University of Tokyo, 2-11-16 Yayoi, Bunkyo-ku, Tokyo, Japan

*Correspondence: miyag-tky@umin.ac.jp

ABSTRACT

The strength of the DNA damage checkpoint critically influences cell fate, yet the mechanisms behind the fine tuning of checkpoint strength during the DNA damage response (DDR) are poorly understood. Here, we show that Rad54B — a SNF2 helicase-like DNA-repair protein — limits the strength of both the G1/S and G2/M checkpoints. We find that Rad54B functions as a scaffold for p53 degradation via its direct interaction with the MDM2-MDMX ubiquitin-ligase complex. During the early phases of the DDR, Rad54B is upregulated, thereby maintaining low checkpoint strength and facilitating cell cycle progression. Once the p53-mediated checkpoint is established, Rad54B is downregulated, and high checkpoint strength is maintained. Constitutive upregulation of Rad54B activity, which is frequently observed in tumors, promotes genomic instability due to checkpoint override. Thus, the scaffolding function of Rad54B dynamically regulates the maintenance of genome integrity by limiting checkpoint strength.

INTRODUCTION

DNA damage responses (DDRs) play critical roles in maintenance of homeostasis, as exemplified by the findings that diverse human diseases, including cancer, are caused by deficiencies in DDR components[1]. The response to DNA double-strand breaks (DSBs) consists of both positive and negative regulatory pathways, which transmit their signals from sensors to effectors to execute cellular responses. These pathways are composed of proteins involved in post-translational modification, such as phosphorylation and ubiquitination. Accumulating evidence suggests that scaffold-like proteins, such as those harboring BRCT domains[2], are involved in the signal transduction pathways of DDRs by recruiting various components and regulators. A recent study has revealed that DNA repair scaffolds directly modulate the checkpoint signaling pathway in budding yeast[3]. Therefore, the functions of scaffold-like proteins in the DDR play essential roles in the coordination of cellular responses to maintain homeostasis.

Human Rad54B was initially identified as a homolog of human Rad54, a central effector of homologous recombination (HR), and mutations in its gene have been observed in primary cancers[4]. Rad54B and Rad54 belong to a subfamily of double-stranded DNA-dependent ATPases referred to as the SWI2/SNF2 family, which is characterized by conserved helicase-like sequence motifs[5]. Although previous studies suggested that Rad54B plays roles in the HR and DNA repair processes[6,7,8,9], biochemical analysis has shown that Rad54B is a less active DNA-dependent ATPase than Rad54[10]. In addition, in contrast to Rad54, the ATPase activity of Rad54B is not

enhanced by the presence of Rad51 and single-stranded DNA. These observations led us to hypothesize that Rad54B plays unknown roles aside from HR repair.

During the cellular response to DNA damage, the choice between cell cycle arrest and progression is critical to the determination of the cell fate. However, despite the importance of the choice, the mechanisms by which this choice is modulated are poorly understood. Here, we show that the SNF2-like domain of Rad54B serves as a scaffold for p53 degradation by facilitating MDM2-MDMX-mediated ubiquitination. Rad54B, whose levels are dynamically regulated in response to DNA damage, regulates the choice between cell cycle arrest and progression by fine-tuning the expression levels of p53. These data suggest that the scaffolding function of Rad54B plays an essential role in the coordination of cellular responses after DNA damage.

RESULTS

Rad54B is a novel DNA damage-responsive protein

First, we examined how Rad54B levels are regulated during the DDR. We found that the levels of Rad54B dynamically changed in response to the genotoxic stresses (Fig. 1a and Supplementary Fig. 1a). Because it appeared that the change in the levels of Rad54B negatively correlated to those of p53, we examined whether p53 is involved in the regulation of the Rad54B levels. Rad54B was transcriptionally suppressed by p53 at a late time point after DNA damage (Fig. 1b). In addition, the Rad54B protein and mRNA levels were suppressed by Nutlin-3-mediated p53 induction (Fig. 1c), suggesting that this transcriptional repression mechanism was independent of p53

4

modification upon DNA damage. Some p53-repressed targets are regulated by the

cyclin–dependent kinase inhibitor p21[11]. However, the repression of Rad54B by p53

was not mediated by p21 (Supplementary Fig. 1b).

To investigate the mechanism underlying Rad54B induction at early time

points after DNA damage, we analyzed cell lines that lack functional p53 (HT-29 and

H1299). Although the decreases in Rad54B expression at the late time points were not

observed in these cell lines, Rad54B expression was significantly increased at the

transcriptional level at the early time points (Figs. 1d,e and Supplementary Figs. 1c-e).

We also found that this induction of Rad54B expression was independent of the activity

of ATM, although the timing of this induction appeared to be delayed by ATM

inhibition (Fig. 1f and Supplementary Fig. 1f). Thus, Rad54B is transcriptionally

induced during the early phases of the DDR independently of the activity of ATM and

is transcriptionally repressed as the p53 levels increase.

Rad54B suppresses the p53 levels independently of ATM

Although previous studies suggest that Rad54B plays roles in the HR and DNA repair

processes[6,7], we found a completely novel function of Rad54B; Rad54B suppressed the

p53 levels and functions in the steady state independently of the activity of ATM (Figs.

1g,h and Supplementary Figs. 1g,h). Although MDM2 is a well-characterized negative

regulator of p53, p53 upregulation was detected even though MDM2 was upregulated

(Supplementary Fig. 1g), suggesting that MDM2 does not efficiently act as a negative

regulator of p53 in the absence of Rad54B. Rad54B repressed the p53 levels and

functions even after the genotoxic stresses, which was also independent of the ATM

activity (Figs. 1i,j and Supplementary Figs. 2a-c). Interestingly, the levels of

phosphorylated p53 were increased in Rad54B-knockdown cells in parallel with the p53

upregulation, whereas the upstream DDRs were not enhanced (Supplementary Fig. 2d).

Furthermore, the amount of DNA damage during the DDR upon oxaliplatin treatment,

as measured by focus formation of γH2AX or 53BP1, was not affected by Rad54B

inhibition (Fig. 1k and Supplementary Fig. 2e). Thus, our data suggest that Rad54B

inhibition upregulates the p53 levels and functions without increasing the amount of

DNA damage. One previous study reported apparently contradictory results regarding

the activity of p53 in Rad54/Rad54b double-knockout cells[12]. However, the findings of

Mahabir et al. do not contrast with our results due to differences in the genotype of the

cells used and in the experimental conditions, particularly the level of DNA damage

induced. In their study, the treated cells exhibited 80% survival, whereas in our study,

the treated cells exhibited 10% or less survival.

The stability of the p53 protein was dramatically increased by Rad54B

knockdown (Fig. 1l and Supplementary Fig. 3a). In addition, we detected a reduction in

endogenous p53 ubiquitination in Rad54B-knockdown cells (Fig. 1m and

Supplementary Fig. 3b). One known mechanism by which p53 is stabilized involves the

alteration of the localization of the negative regulator MDM2 from the nucleus to the

nucleolus[13]. We found that the MDM2 localization pattern, i.e., localization

predominantly in the nucleoplasm and very low expression in the nucleolus or

cytoplasm, was not altered by Rad54B knockdown (Supplementary Fig. 3c). Another

mechanism by which p53 is stabilized is the destabilization of the p53-MDM2 complex[14]. We found that the amount of MDM2 that co-immunoprecipitated with p53 was not reduced by Rad54B knockdown (Supplementary Fig. 3d). These data suggested that Rad54B regulates p53 via an alternative mechanism. Previous studies reported that MDMX augments the E3 ligase activity of MDM2 by forming a heterodimer with MDM2[15,16]. We examined MDM2-MDMX heterodimer formation in Rad54B-knockdown cells. The amount of MDMX that bound to MDM2 was reduced by Rad54B knockdown, even after oxaliplatin treatment (Fig. 1n and Supplementary Figs. 3e,f), indicating that Rad54B regulates the heterodimerization between MDM2 and MDMX, thereby enhancing its ubiquitin ligase activity on p53, which we designate the Rad54B-p53 axis. Therefore, Rad54B appears to enhance the ubiquitin ligase activity of MDM2 on p53 by promoting MDM2-MDMX heterodimerization and counteracts the ATM-mediated positive regulation of p53 (Fig. 1o).

Rad54B directly interacts with MDM2 and MDMX

To clarify how Rad54B promotes MDM2-MDMX heterodimerization, we examined whether Rad54B interacts with MDM2 and MDMX. Exogenous Rad54B interacted with exogenous MDM2 and MDMX in Cos7 cells (Figs. 2a,b). In addition, an interaction between endogenous Rad54B and MDM2 was detected in several human cell lines, including the p53-inactive cell line HeLa (Fig. 2c and Supplementary Figs. 4a,b), indicating that Rad54B and MDM2 universally form a complex independent of the p53 status. We detected an interaction between endogenous Rad54B and MDMX

7

only in the nuclear extract after proteasome inhibition, suggesting that the

Rad54B-MDMX complex exists only transiently in the nucleus (Supplementary Fig. 4c).

The findings that MDM2 knockdown does not affect the levels of Rad54B, as shown

above (Supplementary Fig. 1g), and that Rad54B is not a substrate of proteasomal

degradation (Supplementary Fig. 4d) indicate that the MDM2-Rad54B interaction does

not reflect an enzyme-substrate interaction.

Next, we identified the domains responsible for these interactions. Rad54B is

primarily composed of three domains (Fig. 2d). In Cos7 cells, SNF2-1 was responsible

for the interaction between Rad54B and both MDM2 and MDMX (Figs. 2e,f).

Furthermore, the SNF2-1 protein was pulled down with the GST-MDM2 or

GST-MDMX protein but not with GST alone (Fig. 2g), indicating that the

Rad54B-MDM2 and Rad54B-MDMX interactions are direct. This domain of Rad54B is

characterized by a DExH-box helicase motif and a Walker A nucleotide-binding motif[4].

Although this domain is well conserved among the members of the SWI2/SNF2 family,

including Rad54, Rad54 did not interact with MDM2 (Supplementary Fig. 4e). Our next

interest was to determine whether the ATPase activity of Rad54B plays any role in the

Rad54B-p53 axis. Interestingly, the DExH-box domain of Rad54B (SNF2-1) alone was

sufficient to downregulate p53 (Figs. 2h,i). The crystal structure studies of the

SWI2/SNF2 helicase-like domains of *Sulfolobus solfataricus* Rad54 (SsoRad54) and

zebrafish Rad54 revealed that the N-terminal half of the SWI2/SNF2 helicase-like

domain (DExx-box domain) faces the C-terminal half of the SWI2/SNF2 helicase-like

domain (HELICc domain)[17,18]. Furthermore, mutations in each domain have been

8

shown to affect the double-stranded DNA-dependent ATPase activity of SsoRad54, indicating that both the DExx-box and HELICc domains are required for its catalytic activity[17]. Therefore, the result shown in Fig. 2i suggests that Rad54B likely regulates p53 in an ATPase activity-independent manner. Thus, the DExH-box domain of Rad54B not only contributes to the ATPase activity but also functions as an interface for protein-protein interaction.

MDM2 is composed of four domains (Fig. 2j). With respect to the Rad54B-binding site in MDM2, deletion of the p53-binding domain, the zinc finger domain, and the RING finger domain did not affect the interaction between MDM2 and Rad54B, but deletion of the acidic domain caused a loss of the interaction (Fig. 2k). Therefore, the acidic domain in MDM2 is responsible for its interaction with Rad54B. Some MDM2 binding partners, such as ARF and YY1, are known to bind to this domain and participate in the negative regulation of p53. However, as shown above (Supplementary Figs. 3c,d), the mechanism underlying the negative regulation of p53 by Rad54B is distinct from that by ARF or YY1.

Because exogenous MDMX expression in cells is known to produce some artifactual results[19], we identified the Rad54B-binding site in MDMX by pull-down assays (Supplementary Fig. 4f). MDMX primarily consists of four domains (Fig. 2l). We identified two Rad54B-binding sites located in the N-terminus of MDMX, one of which is the p53-binding domain (Fig. 2m). These data suggest that Rad54B can bind to MDMX independent of p53.

Rad54B serves as a scaffold for MDM2-MDMX heterodimerization

To determine whether the Rad54B-MDM2 and Rad54B-MDMX interactions are

sufficient for the mechanism underlying the Rad54B-p53 axis, we performed an *in vitro*

ubiquitination assay using recombinant proteins. Consistent with previous reports,

MDMX enhanced the p53 polyubiquitination activity of MDM2 *in vitro* (Fig. 3a, lanes

2, 4). Moreover, p53 polyubiquitination was further enhanced by adding SNF2-1 in

addition to MDMX (Fig. 3a, lanes 3-5), indicating that Rad54B plays a role in the

regulation of p53 polyubiquitination by stimulating MDM2-MDMX heterodimerization

and ligase activity.

Next, we investigated the detailed properties of each complex by pull-down

assays to further elucidate the relationship between Rad54B and the MDM2-MDMX

heterodimer. As shown in Fig. 3b, when the three components GST-MDMX, MDM2,

and SNF2-1 were added to the reaction simultaneously, the amount of MDM2 binding

to GST-MDMX was not increased but rather was reduced, likely because SNF2-1 binds

to both MDM2 and MDMX, thereby disturbing the formation of the MDM2-MDMX

heterodimer. This result suggests that excess SNF2-1 disturbs MDM2-MDMX

heterodimerization by preferentially forming complexes with both MDM2 and MDMX.

In contrast, when MDMX was added after allowing MDM2-SNF2-1 complex formation,

MDMX efficiently bound to MDM2 (Fig. 3c). These data suggest that Rad54B serves

as a scaffold for MDM2-MDMX heterodimerization by recruiting MDMX to MDM2

and facilitates efficient p53 degradation (Fig. 3d).

Rad54B promotes mutagenic adaptation to the G2/M checkpoint

To determine the relevance of Rad54B-mediated p53 regulation in cell fate

determination after DNA damage, we investigated the cell cycle distribution after

induction of DNA damage. We found that the number of cells in the G2/M phase was

increased in *RAD54B* knockout (KO) HCT116 cells after oxaliplatin treatment (Fig. 4a)

and in *RAD54B* KO HCT116 and Rad54B-knockdown A549 cells after ionizing

radiation (IR) (Supplementary Figs. 5a,b). In addition, we confirmed that the phenotype

of increased G2/M arrest in *RAD54B* KO cells was rescued by introducing

GFP-conjugated Rad54B (Fig. 4b and Supplementary Fig. 5c). Interestingly, the

increase in G2/M-arrested *RAD54B* KO cells after oxaliplatin treatment was dependent

on the p53 levels (Fig. 4c). These findings indicated that the G2/M checkpoint strength

is reduced by the Rad54B-p53 axis. Notably, aneuploidy was increased by oxaliplatin

treatment in wild-type HCT116 cells (Fig. 4a). In addition, the number of *RAD54B* KO

cells in sub-G1 was decreased after oxaliplatin treatment (Fig. 4a). We confirmed that

this result was due to a reduction in apoptotic cells (Supplementary Fig. 5d). Therefore,

because most *RAD54B* KO cells are strongly arrested at the G2 phase, aneuploidy or

apoptosis arising after release from this arrest appears to be decreased.

As for inactivation of the G2/M checkpoint, previous studies showed that some

cells with unrepaired DNA damage escape from the G2/M checkpoint and enter the next

cell cycle phase. This process of overriding the G2/M checkpoint, referred to as

adaptation, was first described in *Saccharomyces cerevisiae*[20] and was recently

observed in higher eukaryotes, including *Xenopus* cells[21] and even human cancer cells[22].

Thus, we examined whether the Rad54B-dependent abrogation of the G2/M checkpoint observed in wild-type HCT116 cells was accompanied with the cells which undergo adaptation. First, as shown in Fig. 4d, the number of *RAD54B* KO cells that underwent G2/M transition from 12 to 24 hours after oxaliplatin addition was significantly reduced, consistent with the results in Fig. 4a, and this phenotype was rescued by p53 knockdown (Fig. 4e). Next, we examined whether the G2/M transition observed in wild-type cells was accompanied with DNA damage. Surprisingly, approximately 30% to 40% of the wild-type cells in mitosis displayed rigid γH2AX foci when treated with oxaliplatin (Fig. 4f). Furthermore, we found that adaptation was frequently accompanied by chromosomal fragmentation (Fig. 4g). Such fragmentation is highly mutagenic because it can lead to micronucleus formation and loss or translocation of chromosomes. These data suggest that the absolute number of cells which undergo adaptation is increased by Rad54B-mediated inactivation of the G2/M checkpoint. Overall, our data suggest that Rad54B induces highly mutagenic chromosome instability by promoting adaptation.

Rad54B limits the strength of the G1/S checkpoint

Next, we assessed cell morphology after treatment with genotoxic drugs for approximately one week (Fig. 5a). After oxaliplatin treatment, the *RAD54B* KO cells were more likely to remain attached to the dish without any appearance of cell division. 5-FU treatment produced similar results, except that evident and countable colonies were not formed after 5-FU treatment. Based on this finding, we hypothesized that

12

Rad54B regulates the strength of the G1/S checkpoint as well as that of the G2/M checkpoint. Indeed, the strength of the G1/S checkpoint after 5-FU or oxaliplatin treatment was increased by *RAD54B* KO in HCT116 cells (Fig. 5b and Supplementary Fig. 6a) and by Rad54B knockdown in LoVo cells (Supplementary Fig. 6b), which appeared to be partially attributed to the upregulation of the cyclin-dependent kinase inhibitor p21 (Supplementary Fig. 6c). Notably, aneuploidy was increased by 5-FU treatment in wild-type HCT116 cells (Fig. 5b). Furthermore, we detected a decrease in the intake of nucleotides in *RAD54B* KO cells approximately 48 hours after the initiation of 5-FU treatment (Supplementary Fig. 6d). Importantly, the phenotype of the decrease in the number of S-phase cells was rescued by p53 knockdown in *RAD54B* KO cells (Fig. 5c), suggesting that the Rad54B-p53 axis plays critical roles in the regulatory mechanism responsible for inactivation of the G1/S checkpoint.

Proliferation under DNA-damaged conditions increases the probability of genomic instability and mutagenesis. Thus, we examined the impact of Rad54B overexpression on the normal cell line RPE and found that Rad54B overexpression reduced the p53 levels after 5-FU or oxaliplatin treatment (Supplementary Figs. 6e,f). Furthermore, the number of G1-arrested RPE cells after either 5-FU or oxaliplatin treatment was reduced by introduction of the GFP-Rad54B protein (Figs. 5d,e). These data suggest that Rad54B overexpression in normal cells limits the G1/S checkpoint strength, thereby promoting cell cycle progression under DNA-damaged conditions.

To further investigate the roles of Rad54B in the G1/S transition, we examined cells synchronized in the G0/G1 phase by serum starvation or contact inhibition. As

expected, cell cycle progression after IR was delayed in G0/G1 phase-synchronized

RAD54B KO HCT116 and Rad54B-knockdown RPE cells (Figs. 5f,g and

Supplementary Fig. 6g). Furthermore, the G1/S checkpoint strength after IR was

dependent on the p53 levels (Fig. 5h), supporting our hypothesis that the Rad54B-p53

axis plays a critical role in the G1/S checkpoint strength.

Rad54B is a possible therapeutic target for cancer

Based on *in vitro* colony formation assays, we found that the wild-type cells formed

more colonies than the *RAD54B* KO cells (Fig. 6a). These data suggest that the

reduction of the checkpoint strength by Rad54B confers a chance of long-term cell

survival. To investigate this effect *in vivo*, we employed a xenograft model using nude

mice. The *RAD54B* KO cell-derived xenografts grew more slowly than the wild-type

cell-derived xenografts after either oxaliplatin or 5-FU treatment (Fig. 6b). Furthermore,

the number of S-phase cells was reduced in *RAD54B* KO cell-derived xenografts

compared to the wild-type cell-derived xenografts (Fig. 6c), suggesting that G1/S

checkpoint regulation affects xenograft growth. Therefore, Rad54B inhibition enhances

the sensitivity of tumor to genotoxic drugs.

Finally, we investigated the contribution of Rad54B to the neoplastic process.

We selected datasets from the Gene Expression Omnibus database provided by NCBI

(http://www.ncbi.nlm.nih.gov/geo/) and used these data to compare the expression

levels of Rad54B between normal and tumor samples. As shown in Fig. 6d, Rad54B

expression was elevated in many different types of solid tumors. In addition, the two

datasets that provided paired expression data between normal and neoplastic samples from the same patient revealed that all of the samples from colorectal adenoma and 80% of the samples from lung squamous carcinoma displayed elevated Rad54B expression (Fig. 6e and Supplementary Table 1). Notably, enhanced Rad54B expression was observed even in the early stage of the neoplastic process. Furthermore, brain tumor patients displaying elevated Rad54B expression exhibited extremely poor prognosis according to the Kaplan-Meier curve analysis using the REpository for Molecular BRAin Neoplasia DaTa (REMBRANDT) (Fig. 6f; http://caintegrator.nci.nih.gov/rembrandt/). Therefore, these results suggested that elevated Rad54B expression exacerbates clinical outcomes.

Our model shown above suggests that the association between elevated Rad54B expression and the neoplastic process may be dependent on p53 protein function. However, unfortunately, none of the above databases includes any information regarding the mutation status. Therefore, according to a previous study[23], we predicted the mutation status of the samples based on their gene expression patterns, as described in detail in the Methods section. We examined breast cancer (GDS2250), colon adenoma (GDS2947), and glioblastoma (REMBRANDT) samples and found no significant association between the predicted p53 status and the Rad54B expression pattern (Supplementary Figs. 7-9, Supplementary Tables 2 and 3). Overall, these database analyses indicate that the Rad54B-p53 axis plays critical roles in the neoplastic overprocess.

Discussion

Upon DNA damage, the sequential recruitment and activation of the DDR proteins ensure the proper choice of cell fate[1]. The timing of activation of each DDR protein varies from a few minutes to a few days after DNA damage. For example, the recruitment of the DNA-damage marker γH2AX peaks within a few hours after DNA damage, whereas the accumulation of p53 peaks at later time points. Therefore, it has been assumed that negative-regulatory mechanisms for the DDR during its early phases play a role in the coordination of cellular responses[24]. In this study, we demonstrated that the DNA damage-responsive scaffold protein Rad54B constitutes the ATM-independent negative-regulatory DDR pathway; Rad54B is upregulated during the early phases of the DDR to limit p53 activation and is downregulated during the late phases of the DDR to stably induce p53-mediated responses (Fig. 1o). This transcription- and ubiquitination-dependent signaling, in parallel with the phosphorylation-mediated signaling regulated by ATM, causes the latency of p53-mediated checkpoint activation (Fig. 7a). Imbalanced upregulation of Rad54B function promotes genomic instability via G1/S checkpoint override and adaptation to the G2/M checkpoint (Fig. 7b). Our discovery of this exquisite mechanism of p53 regulation via the scaffolding function of Rad54B provides the potential for a novel cancer therapy. Inhibition of Rad54B upregulates the p53 levels without increasing apoptosis even after treatment with genotoxic drugs (Supplementary Fig. 10). In addition, we emphasized the potential advantages of Rad54B inhibition-mediated therapy for targeting tumors at the earlier stages of the neoplastic process (Figs. 5d,e,

and 6e). Thus, Rad54B inhibition, in combination with administration of

DNA-damaging agents, may represent a feasible intervention for p53-reactivating

cancer therapy.

Although the association between the checkpoint strength and cellular

consequences is complex, we assumed that it primarily depends on the type of DNA

damage. As shown in this study, Rad54B broadly limits the checkpoint strength

regardless of the cell type and the type of DNA damage (Figs. 4a, 5b,d-g,

Supplementary Figs. 5a,b, and 6b). On the other hand, the long-term cell survival rate

varies depending on the type of DNA damage; *RAD54B* KO cells are slightly resistant

to IR[6], but they are sensitive to oxaliplatin or 5-FU treatment (Fig. 6a-c). Cell cycle

progression under DNA-damaged conditions results in cell death in most cases, but in

some cases, it confers a chance of cell survival. These contradicting aspects of cell cycle

progression after DNA damage appear to explain these apparently contradicting results.

As for the biological significance of limiting the checkpoint strength, we speculated that

some types of DNA damage, such as that caused by an imbalance of the nucleotide pool

or DNA cross-linking, might not be repaired during checkpoint arrest because such

"potential" DNA damage does not manifest until the cell cycle progresses to

proliferative phases. Therefore, the repair protein Rad54B likely contributes to the

mechanism for cell cycle progression to enable this dormant damage to manifest and to

be repaired. Overall, the scaffolding function of Rad54B, by limiting the checkpoint

strength, coordinates cell fate determination during the DDR.

17

METHODS

Cell culture and antibodies

All cell lines were cultured in a 37°C incubator at 5% CO_2. The A549 and RPE cells

were obtained from RIKEN Cell Bank and Clontech, respectively. The U2OS, HCT116,

and H1299 cells were obtained from ATCC. The HT-29 cells, HCT116 cells, and their

derivatives were cultured in McCoy's 5A medium. The RPE cells were cultured in

DMEM/F-12 medium. The H1299 cells were cultured in RPMI-1640 medium. All other

cell lines were cultured in DMEM medium. All media were supplemented with 10%

fetal bovine serum. The *RAD54B*-KO HCT116 cells were previously described[6].

MG132 (C2211) and cycloheximide (C4859) were obtained from Sigma-Aldrich.

Oxaliplatin and 5-FU were obtained from Wako. Nutlin-3 and the ATM inhibitor were

obtained from Millipore. For irradiation, an X-ray generator (Pantak HF 350:

Shimadzu) was used. For synchronization in the G0/G1 phase, the cells were cultured in

serum-free medium for two days. The antibodies used in this study are shown in

Supplementary Table 5.

Plasmids

The plasmids for FLAG-tag or HA-tag fusion were generated by annealing

oligonucleotides and ligating these regions to pcDNA3.1/Zeo or pEF4/His (Invitrogen),

respectively. The plasmid for GFP fusion was generated by PCR amplification followed

by cloning into the MMTV promoter-based plasmid. The plasmids for full-length

human Rad54B and Rad54 were previously described[25]. The plasmid for flow

18

cytometric analyses was generated by inserting the Rad54B coding region into the

pIRES2-EGFP vector (Clontech). The plasmids encoding full-length human MDM2,

MDMX, or p53 were cloned by PCR from HEK293 or RPE cell cDNA. The Rad54B,

MDM2, or MDMX fragment expression plasmids were generated by PCR. The

sequences of all PCR products were confirmed. For GST-tagged or 6×His-tagged

proteins, the coding sequence of each protein was ligated to pGEX-5X (GE Healthcare)

or pET32a (Novagen), respectively.

Plasmid transfection, immunoprecipitation, and Western blot

The cells were transfected with the indicated plasmids using Lipofectamine^{TM} 2000

reagent (Invitrogen) according to the manufacturer's instructions. For Western blot, the

cells were harvested in lysis buffer (0.5% NP-40, 50 mM Tris-HCl (pH 7.4), 150 mM

NaCl, 0.5 mM EDTA, 1 mM DTT, 1 mM PMSF, 10 μg ml^{-1} aprotinin, 50 nM

cantharidin, and 5 nM Microcystin-LR). For immunoprecipitation, the indicated

antibody was added to the lysate, and the solution was continuously rotated at 4°C.

After two hours, the solution was supplemented with Protein G agarose (Invitrogen) and

rotated for another 1 hour. The beads were washed three times with lysis buffer and

denatured by boiling in SDS sample buffer. The denatured proteins were resolved by

SDS-PAGE and transferred to PVDF membrane (Millipore). Immunoblots were

detected using ECL (GE Healthcare), and the band intensity on the film was quantified

using Image J software. Full scans of the blots are shown in Supplementary Figs. 11 and

12.

mRNA extraction and quantitative RT-PCR

Total RNA was extracted using RNAiso Plus (Takara) according to the manufacturer's

instructions. Extracted RNA was reverse-transcribed using Moloney murine leukemia

virus reverse-transcriptase, ribonuclease inhibitor, and random hexamers (Takara). The

synthesized cDNAs were analyzed for each gene expression level by real-time PCR

using a Smart Cycler PCR system and SYBR Premix Ex Taq^{TM} (Takara) according to

the manufacturer's instructions. The results were quantified relative to a calibration

curve for each primer set and were normalized to the GAPDH levels. All measurements

were performed in triplicate. The following primers were used in this study: GAPDH,

5'-GCACCGTCAAGGCTGAGAAC-3' (forward) and

5'-ATGGTGGTGAAGACGCCAGT-3' (reverse); Rad54B,

5'-TCCAGGTCTGAATGAAGAGATTAC-3' (forward) and

5'-TCTAGTACTTTCTTCACTAGGCAG-3' (reverse); p53,

5'-AGATGTTCCGAGAGCTGAATGAG-3' (forward) and

5'-GAGAATGTCAGTCTGAGTCAGGC-3' (reverse); MDM2,

5'-CCTTAGCTGACTATTGGAAATGC-3' (forward) and

5'-ACATCAAAGCCCTCTTCAGCTTG-3' (reverse); p21,

5'-GACTCTCAGGGTCGAAAACGG-3' (forward) and

5'-GCGGATTAGGGCTTCCTCTTG-3' (reverse); and Bax,

5'-ACTCCCCCCGAGAGGTCTT-3' (forward) and

5'-GCAAAGTAGAAAAGGGCGACAA-3' (reverse).

20

siRNA

All siRNAs were purchased from Dharmacon. Each siRNA (final concentration of 50-75 nM) was transfected into cells using DharmaFECT4 transfection reagent (Dharmacon). For co-transfection of siRNAs and plasmid, siRad54B #2&#3 (final concentration of 40 nM each) and pEF-HA-Rad54B 1-467 or SNF2-1 plasmid were transfected using DharmaFECT Duo transfection reagent (Dharmacon) according to the manufacturer's instructions.

Production of recombinant proteins

The GST fusion proteins were expressed in *E. coli* BL21 cells (GE Healthcare, New England BioLabs) and were purified on an Immobilized Glutathione Column (Thermo Scientific) or Glutathione Sepharose 4B (GE Healthcare) according to the manufacturer's instructions. The 6×His fusion proteins were expressed in BL21(DE3) cells (Invitrogen) and were purified on a TALON resin and a TALON Disposable Gravity Column (Clontech). All proteins were dissolved in binding buffer (20 mM Tris-HCl (pH 7.4), 10 mM NaCl, and 1 mM $MgCl_2$) using Amicon Ultra-0.5 10K (Millipore). If required, the GST tag was removed using Factor Xa (New England BioLabs).

GST pull-down assay

For the GST pull-down assays, the indicated proteins were mixed and incubated at room

temperature. After 1-2 hours, the GST-tagged proteins were pulled down using

Glutathione Sepharose 4B (GE Healthcare) and were eluted in elution buffer (50 mM

Tris-HCl (pH 8.0) and 10 mM glutathione). The products were resolved by SDS-PAGE

and immunoblotted using the indicated antibody.

In vitro ubiquitination assay

In vitro ubiquitination assays were conducted in reaction buffer (50 mM Tris-HCl (pH

7.4), 5 mM $MgCl_2$, 2 mM ATP, and 2 mM DTT) supplemented with human UBE1 (6

nM), human UbcH5b (100 nM) (Boston Biochem), *in vitro* translated p53 (0.3 μl)

(Promega) and MDM2 (100 ng), in the absence or presence of ubiquitin (25 μM)

(Boston Biochem), GST-MDMX (200 ng) and His-SNF2-1 (200 ng) at 37°C for 2 hours.

The reaction was halted by adding SDS sample buffer, and the products were analyzed

by Western blot.

Cell cycle analysis

Cells detached using Trypsin-EDTA were fixed if indicated and were stained using a

CycleTEST^{TM} PLUS DNA Reagent Kit (Becton Dickinson) according to the

manufacturer's instructions. Cell cycle analysis was performed using an EPICS XL

flow cytometer (Beckman Coulter). For the 5-ethynyl-2´-deoxyuridine (EdU) assay,

EdU (Invitrogen; 10 μM) was added to the medium at the indicated time before

harvesting. The harvested cells were fixed in 4% paraformaldehyde for 10 minutes and

were permeabilized using 0.5% Triton-X for 5 minutes at room temperature. After

several washes, the incorporated EdU was labeled for 30 minutes by a click chemistry

reaction in buffer containing 100 mM Tris-HCl (pH 8.0), 1 mM $CuSO_4$, and 10 μM

Alexa 488 azide (Invitrogen) supplemented with 100 mM ascorbic acid. The labeled

cells were stained with propidium iodide (PI) and were analyzed as described above.

Immunofluorescence

The cells cultured on coverslips or detached using Trypsin-EDTA were fixed in 4%

paraformaldehyde for 10 minutes at room temperature. The cells were permeabilized

using 0.5% Triton-X and 0.1% SDS for 5 minutes, followed by blocking with 10%

horse serum for 30 minutes. Then, the cells were incubated in primary antibodies and,

subsequently, in secondary antibodies at 37°C for 30 minutes. For the cells on

coverslips, the cells were counterstained with DAPI and mounted. Representative

images were captured using an Olympus BX51 fluorescence microscope and an

Olympus DP 70 digital camera equipped with an Olympus DP controller and DP

manager software. For the detached cells, the cells were analyzed using a FACSAria II

cell sorter (Becton Dickinson).

Colony formation assay

The wild-type or *RAD54B*-KO HCT116 cells were seeded at a density of 6.0×10^3 cells

per 60 mm dish and were treated with oxaliplatin at the indicated dose. After 7-10 days,

the cells were fixed and stained to count the colonies. All measurements were

performed in triplicate.

Xenograft model

All animal experiments were approved by the Institutional Animal Experiment

Committee of The University of Tokyo. Male BALB/c SIc-nu/nu mice (4 weeks of age)

were purchased from Nihon SLC (Shizuoka, Japan). Then, 2.5×10^6 wild-type HCT116

cells or their derivatives were injected subcutaneously. When the tumors reached

approximately 100 mm^3 (Day 0), the mice were intraperitoneally injected with

oxaliplatin weekly or 5-FU daily at the indicated dose. Tumor growth was measured

every day after initiation of treatment, and the tumor volume was calculated as $0.5 \times$

length $\times$ width^2. For cell cycle analysis, the oxaliplatin-treated mice were euthanized on

Day 2 or 3, and the tumors were homogenized for PI staining, which was performed as

described above.

Analysis of the databases

Using the raw expression data provided by the GEO database, the average and standard

deviation of the Rad54B expression levels in normal and tumor samples were calculated

and were compared using the Mann-Whitney U-test. The average Rad54B expression

levels in tumor samples were normalized to those in normal samples. The gene datasets

for p53 mutation status prediction were identified according to the procedure described

in a previous study[23] with some modifications. Briefly, using the gene expression data

provided by TCGA, the differentially expressed genes between the samples harboring

wild-type and mutant p53 were identified by excluding those genes displaying a *P* value

on Welch's *t*-test >0.001 and by ranking the included genes in decreasing order of the

log ratio. For hierarchical cluster analyses, the gene expression values were

mean-centered, and the genes and the samples were clustered by Pearson correlation

and average linkage (Cluster 3.0 software) to confirm the efficiency of the prediction.

The clustering results were visualized using Java TreeView software. The samples from

GEO or REMBRANDT were assigned to the appropriate cluster using the nearest

neighbor algorithm according to Pearson correlation-based similarity.

REFERENCES

1.   Jackson SP, Bartek J. The DNA-damage response in human biology and disease. *Nature* **461**, 1071-1078 (2009).

2.   Gerloff DL, Woods NT, Farago AA, Monteiro AN. BRCT domains: A little more than kin, and less than kind. *FEBS Lett* **586**, 2711-2716 (2012).

3.   Ohouo PY, Bastos de Oliveira FM, Liu Y, Ma CJ, Smolka MB. DNA-repair scaffolds dampen checkpoint signalling by counteracting the adaptor Rad9. *Nature* **493**, 120-124 (2013).

4.   Hiramoto T*, et al.* Mutations of a novel human RAD54 homologue, RAD54B, in primary cancer. *Oncogene* **18**, 3422-3426 (1999).

5.   Ceballos SJ, Heyer WD. Functions of the Snf2/Swi2 family Rad54 motor protein in homologous recombination. *Biochim Biophys Acta* **1809**, 509-523 (2011).

6.   Miyagawa K*, et al.* A role for RAD54B in homologous recombination in human cells. *EMBO J* **21**, 175-180 (2002).

7. Wesoly J, *et al.* Differential contributions of mammalian Rad54 paralogs to recombination, DNA damage repair, and meiosis. *Mol Cell Biol* **26**, 976-989 (2006).

8. Mahabir AG, *et al.* DNA-repair-deficient Rad54/Rad54B mice are more sensitive to clastogens than wild-type mice. *Toxicol Lett* **183**, 112-117 (2008).

9. Kirshner M, *et al.* Analysis of the relationships between ATM and the Rad54 paralogs involved in homologous recombination repair. *DNA Repair* **8**, 253-261 (2009).

10. Tanaka K, Kagawa W, Kinebuchi T, Kurumizaka H, Miyagawa K. Human Rad54B is a double-stranded DNA-dependent ATPase and has biochemical properties different from its structural homolog in yeast, Tid1/Rdh54. *Nucleic Acids Res* **30**, 1346-1353 (2002).

11. Laptenko O, Prives C. Transcriptional regulation by p53: one protein, many possibilities. *Cell Death Differ* **13**, 951-961 (2006).

12.   Mahabir AG, Schaap MM, Pennings JL, van Benthem J, Hendriksen CF, van

Steeg H. Comparison of clastogen-induced gene expression profiles in wild-type

and DNA repair-deficient Rad54/Rad54B cells. *BMC Genomics* **11**, 24 (2010).

13.   Zhang Y, Xiong Y. Control of p53 ubiquitination and nuclear export by MDM2

and ARF. *Cell Growth Differ* **12**, 175-186 (2001).

14.   Sui G*, et al.* Yin Yang 1 is a negative regulator of p53. *Cell* **117**, 859-872

(2004).

15.   Tanimura S, Ohtsuka S, Mitsui K, Shirouzu K, Yoshimura A, Ohtsubo M.

MDM2 interacts with MDMX through their RING finger domains. *FEBS Lett*

447, 5-9 (1999).

16.   Linares LK, Hengstermann A, Ciechanover A, Muller S, Scheffner M. HdmX

stimulates Hdm2-mediated ubiquitination and degradation of p53. *Proc Natl*

Acad Sci USA **100**, 12009-12014 (2003).

17.   Durr H, Korner C, Muller M, Hickmann V, Hopfner KP. X-ray structures of the

Sulfolobus solfataricus SWI2/SNF2 ATPase core and its complex with DNA.

Cell **121**, 363-373 (2005).

18.   Thoma NH, Czyzewski BK, Alexeev AA, Mazin AV, Kowalczykowski SC,

        Pavletich NP. Structure of the SWI2/SNF2 chromatin-remodeling domain of

        eukaryotic Rad54. *Nat Struct Mol Biol* **12**, 350-356 (2005).

19.   Marine JC, Jochemsen AG. Mdmx as an essential regulator of p53 activity.

        Biochem Biophys Res Commun **331**, 750-760 (2005).

20.   Toczyski DP, Galgoczy DJ, Hartwell LH. CDC5 and CKII control adaptation to

        the yeast DNA damage checkpoint. *Cell* **90**, 1097-1106 (1997).

21.   Yoo HY, Kumagai A, Shevchenko A, Shevchenko A, Dunphy WG. Adaptation

        of a DNA replication checkpoint response depends upon inactivation of Claspin

        by the Polo-like kinase. *Cell* **117**, 575-588 (2004).

22.   Syljuasen RG, Jensen S, Bartek J, Lukas J. Adaptation to the ionizing

        radiation-induced G2 checkpoint occurs in human cells and depends on

        checkpoint kinase 1 and Polo-like kinase 1 kinases. *Cancer Res* **66**,

        10253-10257 (2006).

23.   Miller LD, *et al.* An expression signature for p53 status in human breast cancer predicts mutation status, transcriptional effects, and patient survival. *Proc Natl Acad Sci USA* **102**, 13550-13555 (2005).

24.   Panier S, Durocher D. Push back to respond better: regulatory inhibition of the DNA double-strand break response. *Nat Rev Cancer* **13**, 661-672 (2013).

25.   Tanaka K, Hiramoto T, Fukuda T, Miyagawa K. A novel human rad54 homologue, Rad54B, associates with Rad51. *J Biol Chem* **275**, 26316-26321 (2000).

END NOTES

Author Contributions

KM and TY designed the study. TY performed most of the experiments. TY and TS performed the animal experiments. MK generated the Rad54B fragment constructs and assisted with the flow cytometry experiments. TY and KM analyzed the results and wrote the manuscript.

Competing Financial Interests

The authors declare no competing financial interest.

FIGURE LEGENDS

Figure 1 | Rad54B constitutes a novel negative-regulatory pathway for p53 independently of ATM. (**a**) The responses of Rad54B and p53 expression to oxaliplatin treatment in HCT116 cells harboring wild-type p53. Quantification of each protein level is shown below. (**b**) The contribution of p53 to the reduction in Rad54B after DNA damage (mean ± s.d.). n.s., not significant; * $P<0.05$, two-tailed t-test, n=3. (**c**) The effects of DNA damage-independent p53 induction by Nutlin-3 (10 μM) on Rad54B protein and mRNA expression (mean ± s.d.). * $P<0.05$, two-tailed t-test, n=3. (**d**) Western blot for Rad54B after oxaliplatin treatment or IR of HT-29 cells harboring mutant p53. (**e, f**) The Rad54B mRNA levels after IR and the effects of ATM inhibition (mean ± s.d.). * $P<0.05$, two-tailed t-test, n=3. (**g**) Western blot for p53 after Rad54B inhibition. (**h**) The effects of ATM inhibition on Rad54B-mediated p53 inhibition. (**i**)

Western blot for p53 after DNA damage with Rad54B inhibition. (**j**) The effects of

ATM inhibition on Rad54B-mediated p53 inhibition during the DDR. (**l**) The stability

of the p53 protein after cycloheximide (CHX) treatment (mean ± s.e.m.; n=3). **

P=0.0039, Wilcoxon matched-pairs signed-rank test. (**k**) The number of γH2AX and

53BP1 foci-positive cells at the indicated time points after oxaliplatin treatment and

washing were counted (mean ± s.d.). n.s., not significant; two-tailed Welch's *t*-test, n=5

for each time point. (**m**) Western blot for ubiquitinated p53 after proteasome inhibition

using MG132 (10 μM). (**n**) The MDM2-MDMX complex was analyzed by

immunoprecipitation after 6 hours of proteasome inhibition using MG132 (10 μM). (**o**)

The MDM2-MDMX-mediated ubiquitination-dependent feedback inhibitory loop

between Rad54B and p53. Rad54B counteracts the canonical ATM kinase-mediated

pathway during the DDR.

Figure 2 | Rad54B directly interacts with MDM2 and MDMX. (**a,b**) The

Rad54B-MDM2 and Rad54B-MDMX interactions were detected in Cos7 cells. (**c**) The

interaction between endogenous Rad54B and MDM2. (**d**) Schematic representation of

Rad54B and its fragments. The seven conserved helicase-like motifs found in the SNF2

superfamily are indicated by filled boxes. (**e,f**) The interaction between the SNF2-1

domain and MDM2 or MDMX was confirmed by immunoprecipitation in Cos7 cells.

The arrows indicate each HA-Rad54B fragment, heavy chain (H.C.), or light chain

(L.C.). (**g**) The direct interactions were confirmed by pull-down assays. (**h**) Schematic

representation of Rad54B mRNA and the targeting region of each siRNA. Notably,

neither Rad54B 1-467 nor SNF2-1 expression was interfered using siRNA #2 or #3. (**i**) The effects of supplementation of the Rad54B fragments to the Rad54B-knockdown cells were analyzed. (**j**) Schematic representation of MDM2 and its fragments. (**k**) The interaction between the MDM2 fragments and full-length Rad54B was analyzed by immunoprecipitation in Cos7 cells. (**l**) Schematic representation of MDMX and its fragments. (**m**) The interaction between the MDMX fragment and the Rad54B SNF2-1 fragment was analyzed by pull-down assays.

Figure 3 | Rad54B enhances p53 ubiquitination by recruiting MDMX to MDM2 and promoting MDM2-MDMX heterodimerization. (**a**) *In vitro* ubiquitination assays for p53. (**b**) Pull-down assays in which all indicated proteins were included simultaneously. The Western blot shown below displays the same amount of MDMX in each product. (**c**) Pull-down assays in which the indicated proteins were pre-incubated for 1 hour. The Western blot shown below displays the same amount of MDMX in each product. (**d**) A hypothetical model for the sequence of complex formation in the Rad54B-p53 axis. Upon p53 ubiquitination, either p53 is recruited to the Rad54B-MDM2 complex or Rad54B is recruited to the p53-MDM2 complex. After formation of the Rad54B-MDM2-p53 complex, MDMX is recruited to MDM2 by Rad54B, followed by p53 polyubiquitination and degradation.

Figure 4 | Rad54B promotes mutagenic adaptation by dampening p53-dependent G2/M checkpoint maintenance. (**a**) The number of the cells in the G2/M phase after

oxaliplatin treatment (mean ± s.e.m.; n=3). Representative diagrams are shown in the right panel. n.s., not significant; * *P*=0.019, two-tailed paired *t*-test. (**b**) The cell cycle distributions of the cells transfected with the indicated constructs were analyzed by flow cytometry. The diagrams shown are representative of three independent experiments. (**c**) The number of G2/M-phase p53-knockdown *RAD54B* KO cells after oxaliplatin treatment was measured at the indicated time points. The graph shown is representative of four independent experiments. (**d**) The oxaliplatin-treated cells were supplemented with colcemid (0.1 µg ml⁻¹) 12 hours before measurement of the mitotic index (mean ± s.d.). n.s., not significant; ** *P*<0.001, two-tailed Welch's *t*-test, n=5. (**e**) p53-knockdown *RAD54B* KO cells were analyzed as in (**d**) (mean ± s.d.). ** *P*<0.001, two-tailed Welch's *t*-test, n=10. (**f,g**) The oxaliplatin-treated wild-type cells were supplemented with colcemid 12 hours before fixation and staining with phospho-histone H3 (a mitosis marker) and γH2AX (a DNA damage marker). A representative field is shown. Scale bar, 10 µm. The arrows indicate the fragmentation of chromosomes.

Figure 5 | Rad54B loosens the DNA damage-induced G1/S checkpoint. (**a**) Cell morphology on the indicated day after oxaliplatin or 5-FU treatment. A representative field is shown. Scale bar, 150 µm. (**b**) The cell cycle distributions after 5-FU treatment. The ranges of aneuploid cells are shown below the diagrams. The results are representative of three independent experiments. (**c**) The number of S phase p53-knockdown cells after 5-FU treatment was measured. The results are representative of three independent experiments. (**d,e**) The number of G1-arrested cells after DNA

damage in Rad54B-overexpressing RPE cells was measured (mean ± s.e.m.; n=3). *

$P<0.05$, two-tailed t-test. (**f**) Serum-starved *RAD54B* KO cells were released from cell

cycle arrest by serum addition immediately after IR. The cell cycle distributions were

analyzed at the indicated time points. The results are representative of four independent

experiments. (**g**) Fully confluent Rad54B-knockdown RPE cells were reseeded at low

density immediately after IR. The cell cycle distributions were analyzed at the indicated

time points. The results are representative of three independent experiments. (**h**)

Nutlin-3 was added eight hours before IR and serum addition. The cell cycle

distributions were analyzed at the indicated time points. The results are representative of

three independent experiments.

Figure 6 | Inhibition of Rad54B expression is a feasible strategy for cancer therapy. (**a**)

Colony formation assays after oxaliplatin treatment (mean ± s.e.m.; n=4). * $P=0.0117$,

two-way ANOVA with repeated measures on the log-transformed cell count, $F_{1,3}=30.4$.

(**b**) The xenograft volume after drug injection was analyzed (mean ± s.d., a semi-log

scale). The number of mice observed is shown at the right of each line. * $P<0.05$, **

$P<0.01$, two-tailed Welch's t-test on the log-transformed rate of xenograft volume

growth. (**c**) The cell cycle distributions of the representative xenografts at the indicated

time points were analyzed. (**d**) The Rad54B levels in the neoplastic samples (means ±

s.d.). The number of samples analyzed is shown in Supplementary Table 1. The average

Rad54B levels in tumor samples were normalized to those in normal samples. * $P<0.05$,

** $P<0.01$, Mann-Whitney U-test. (**e**) The paired Rad54B expression data between

normal and colorectal adenoma samples from the same patient. See also Supplementary

Table 1. (**f**) The survival datasets from REMBRANDT. Elevated expression was

defined as a 2-fold or greater increase in Rad54B expression. The points in the graph

correspond to the censored cases. For a detailed description, see the REMBRANDT

website. ** *P*<0.001, log-rank test.

Figure 7 | Schematic summary of this study in terms of the time course and cell cycle.

(**a**) The scaffold protein Rad54B causes the latency of p53-mediated checkpoint

activation. During the early phases of the DDR, Rad54B constitutes the

ATM-independent negative-regulatory DDR pathway. (**b**) The Rad54B-p53 axis

regulates the checkpoint strength. Elevated expression of Rad54B induces checkpoint

override, thereby enhancing genomic instability, mutagenesis and drug resistance.

Figure-1 (Miyagawa)
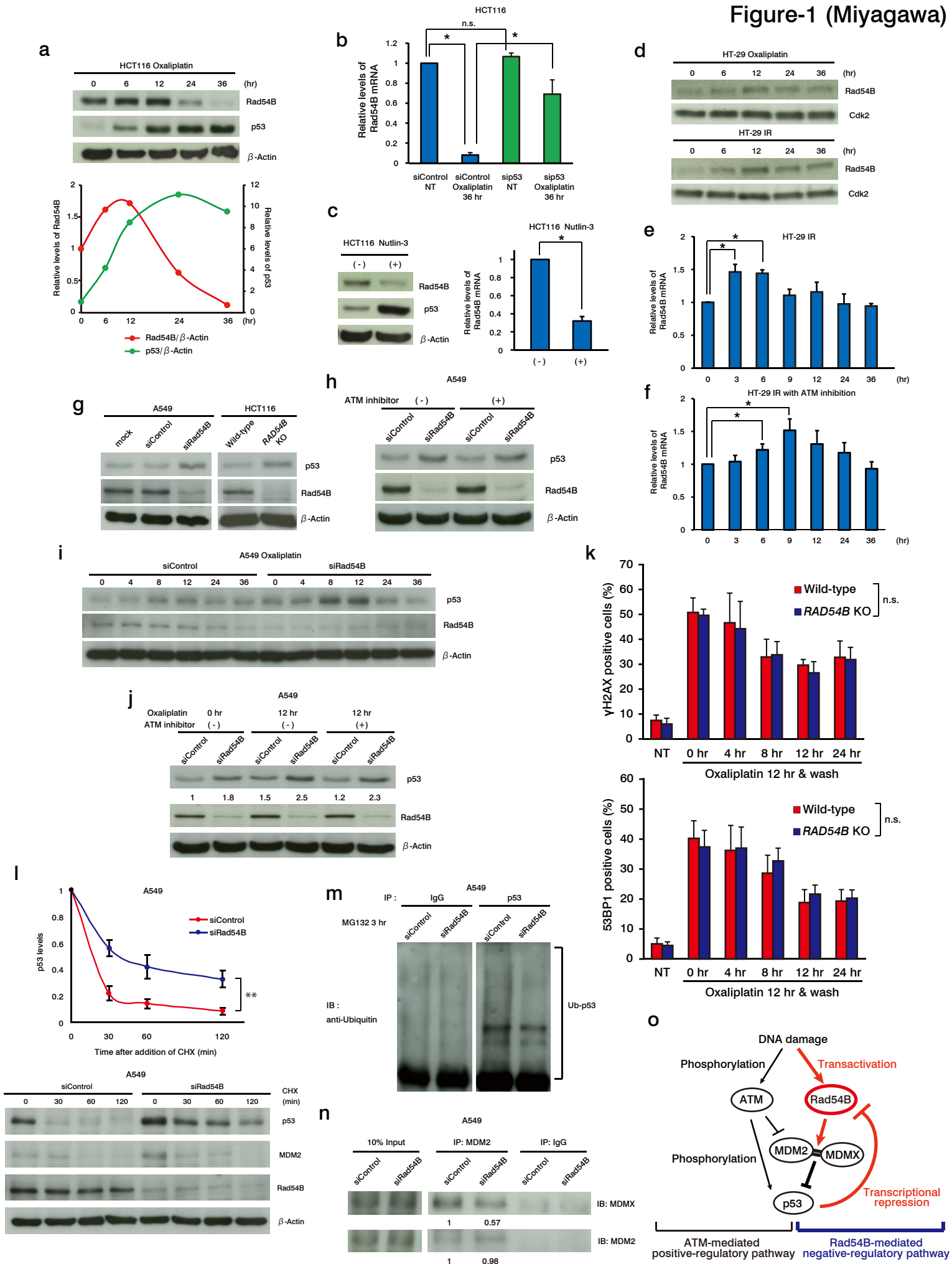
Figure-2 (Miyagawa)
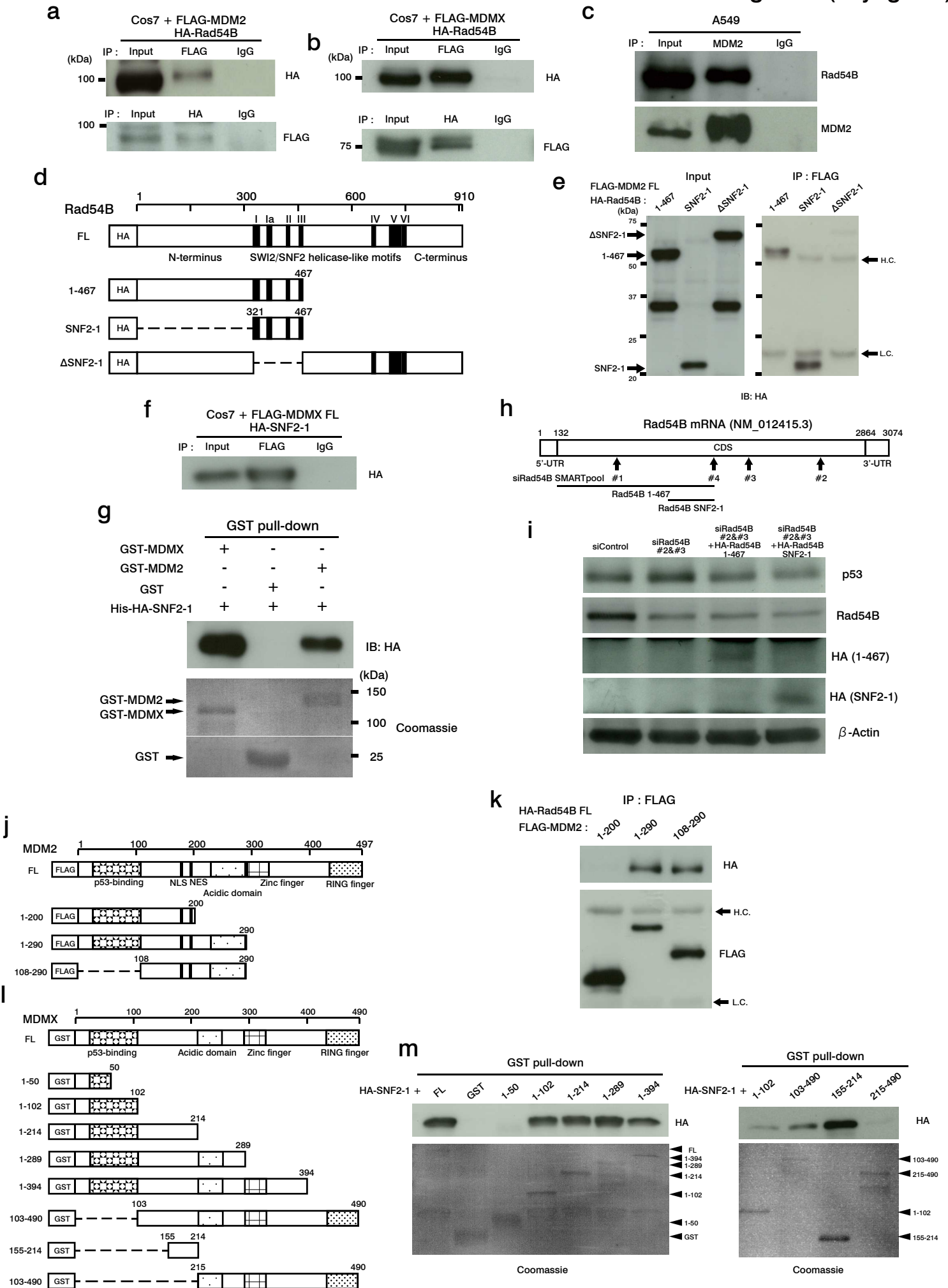
Figure-3 (Miyagawa)
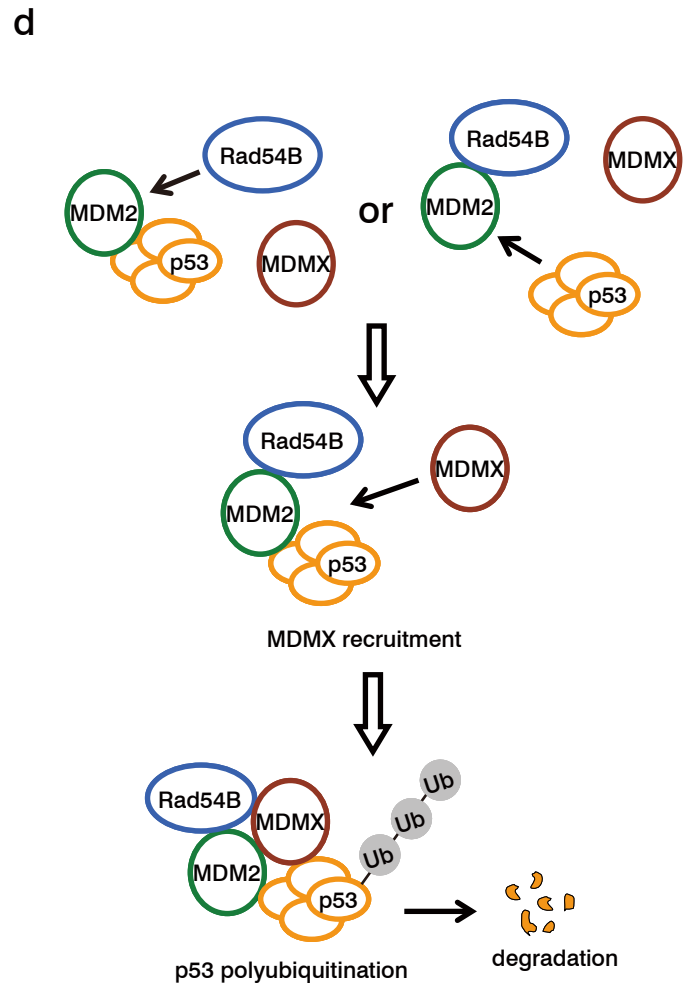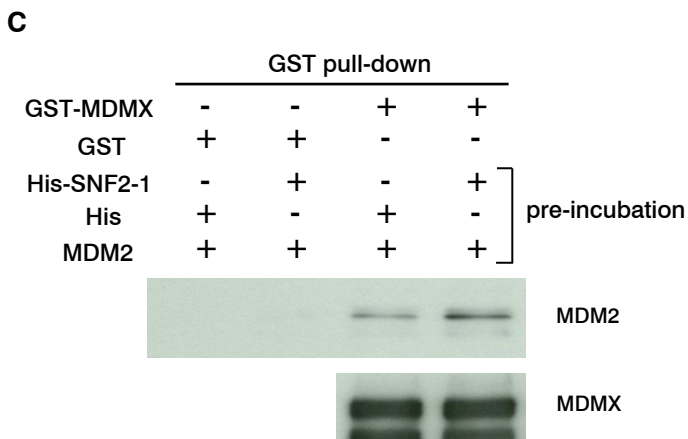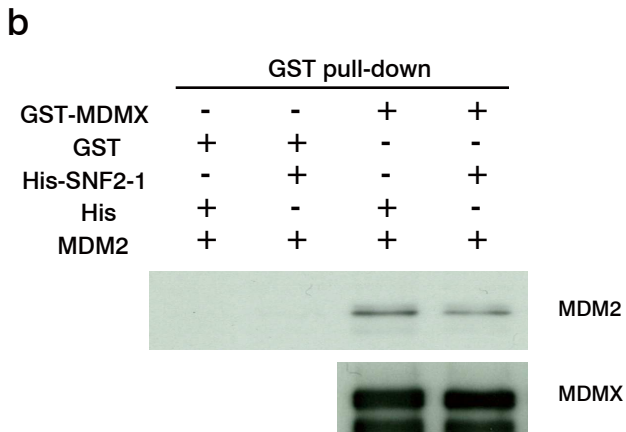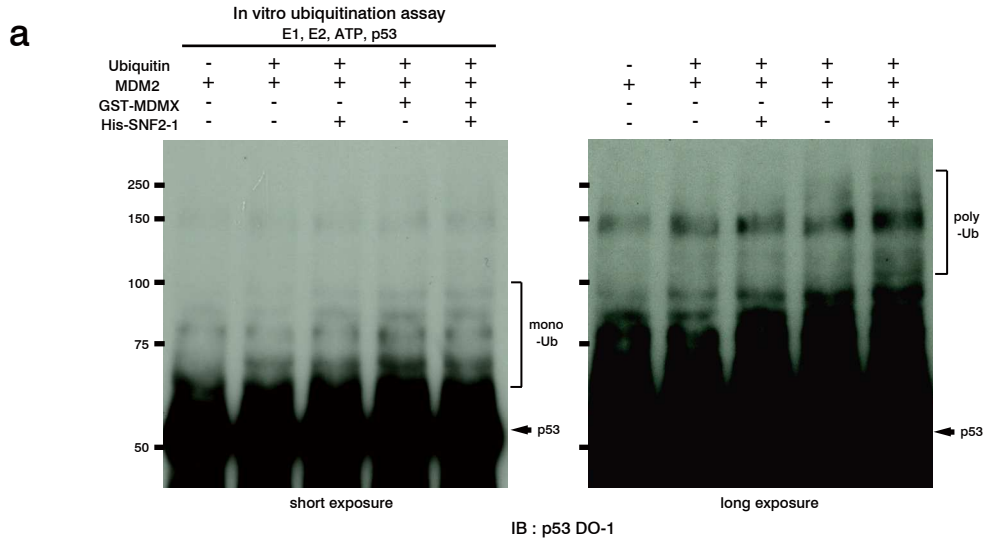
Figure-4 (Miyagawa)
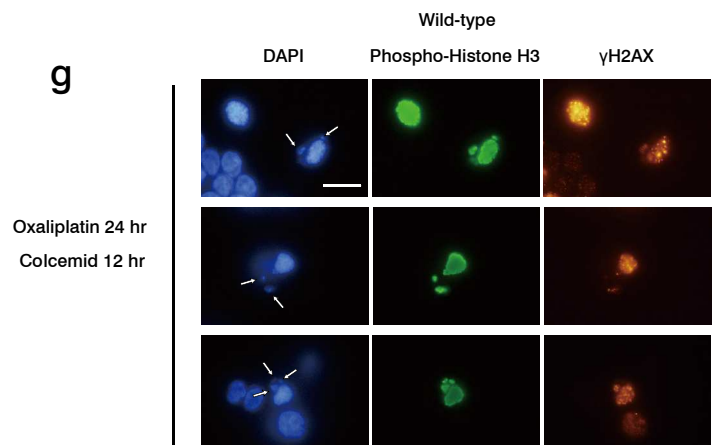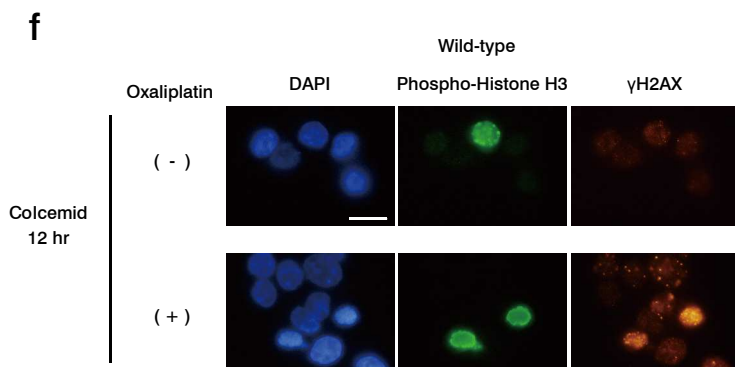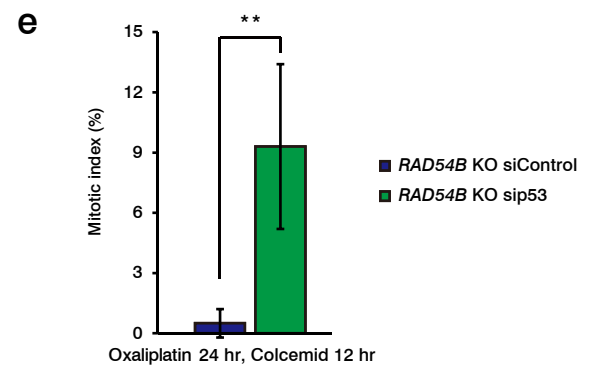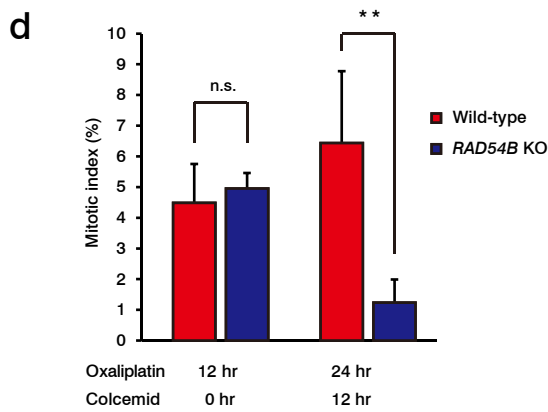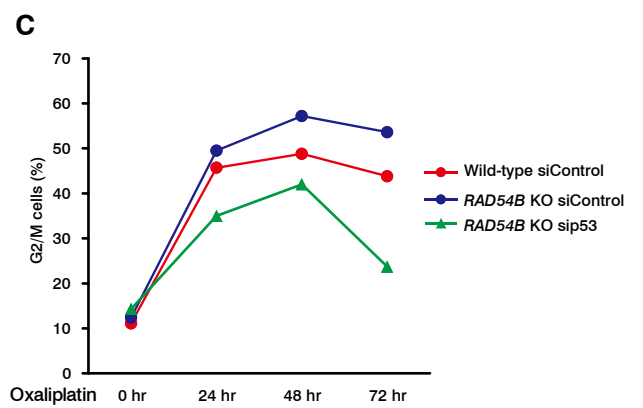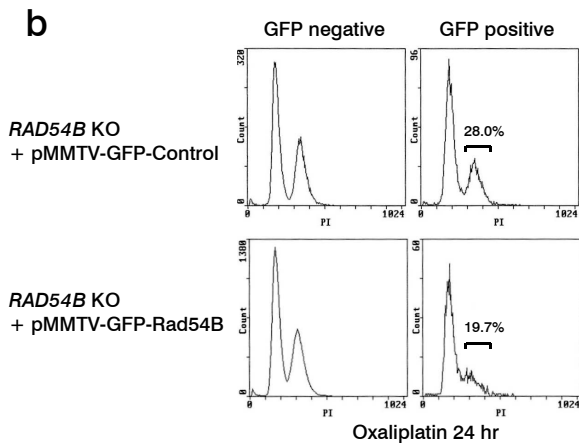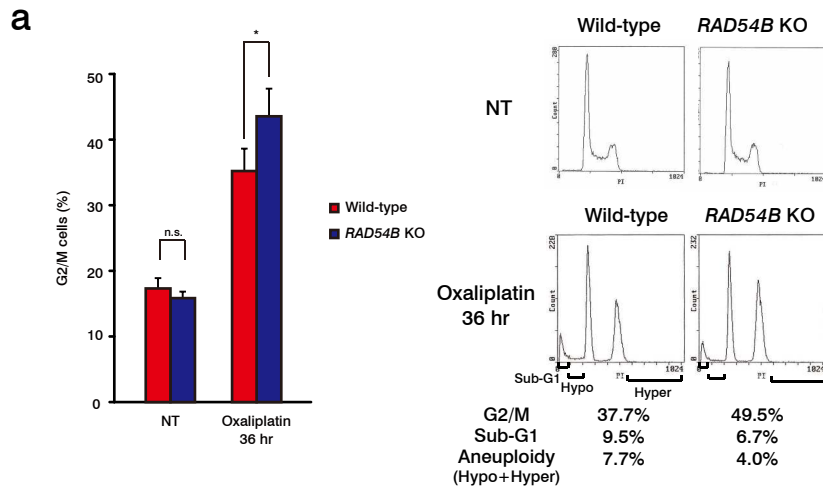
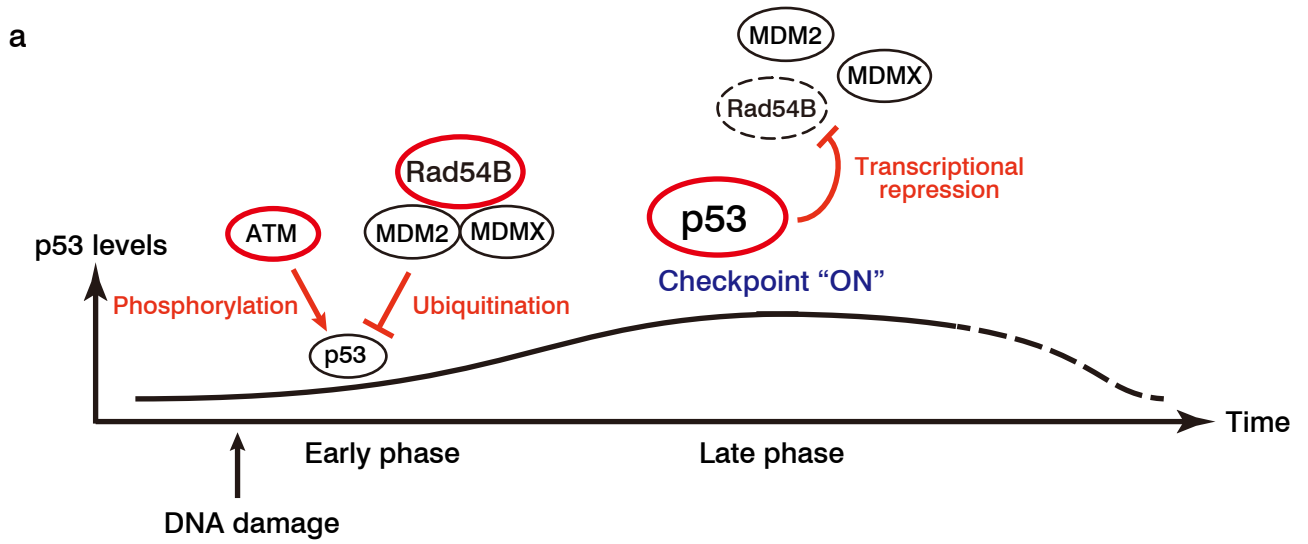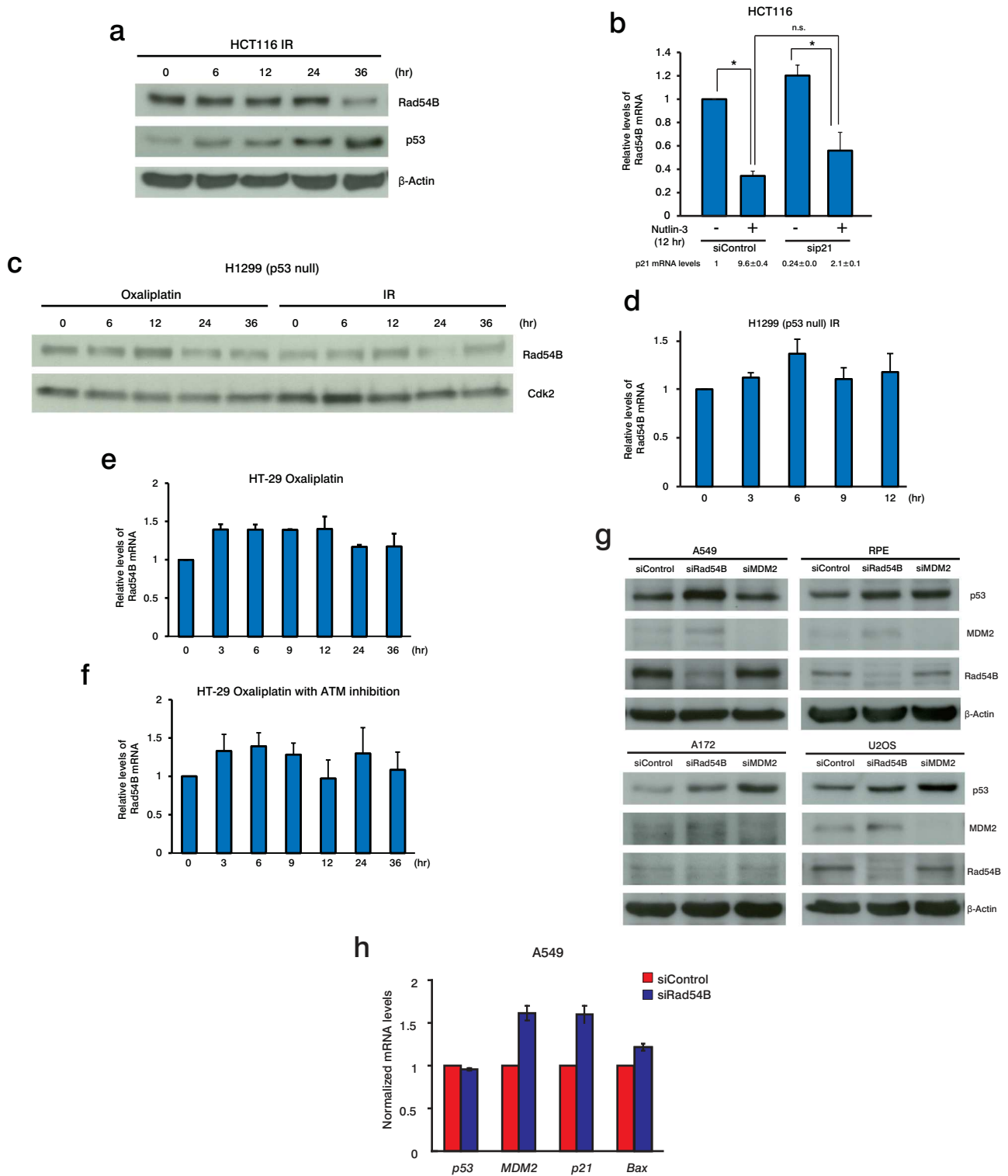Figure-5 (Miyagawa)
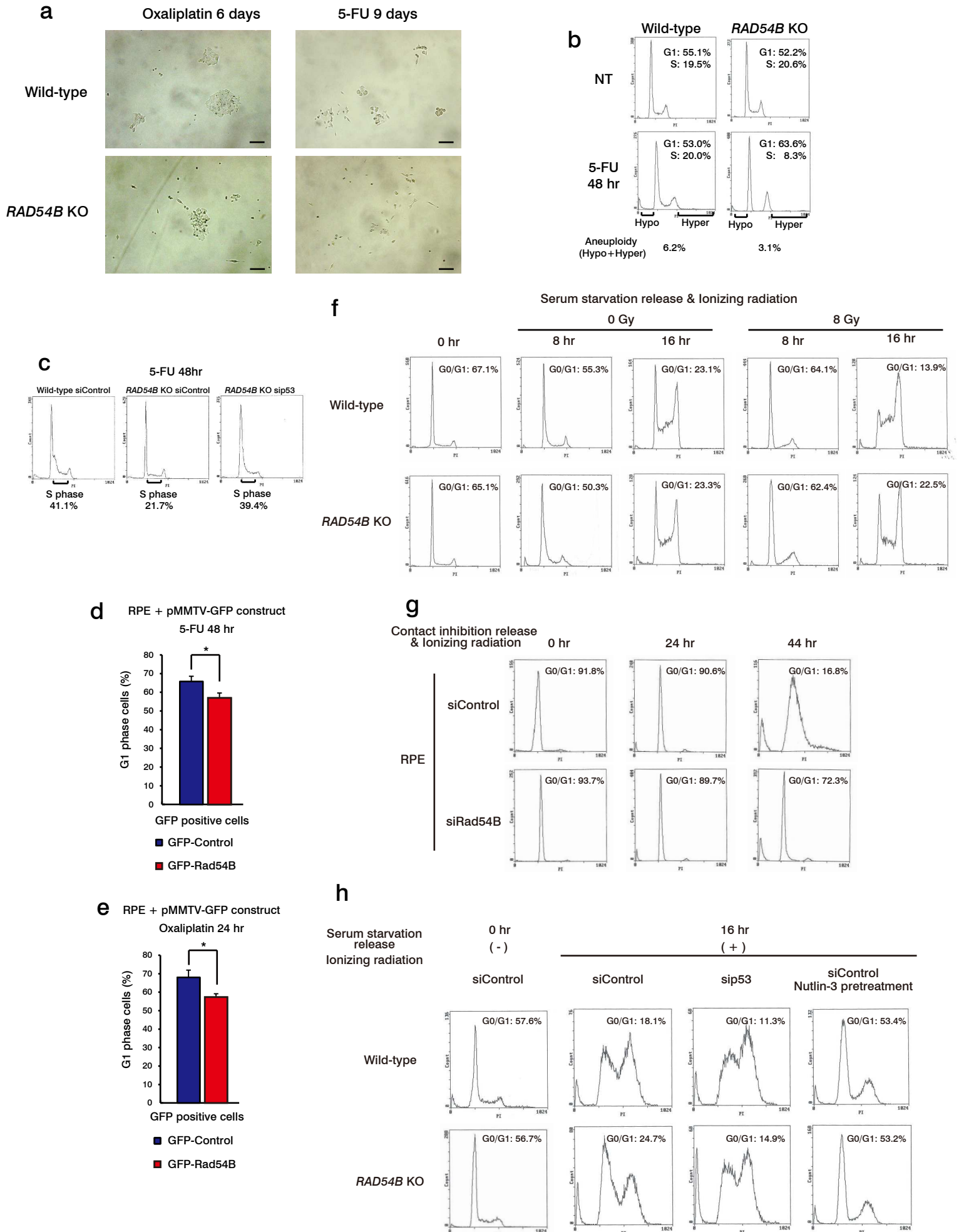
Figure-6 (Miyagawa)
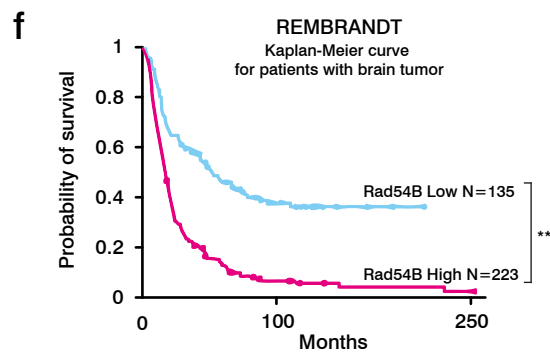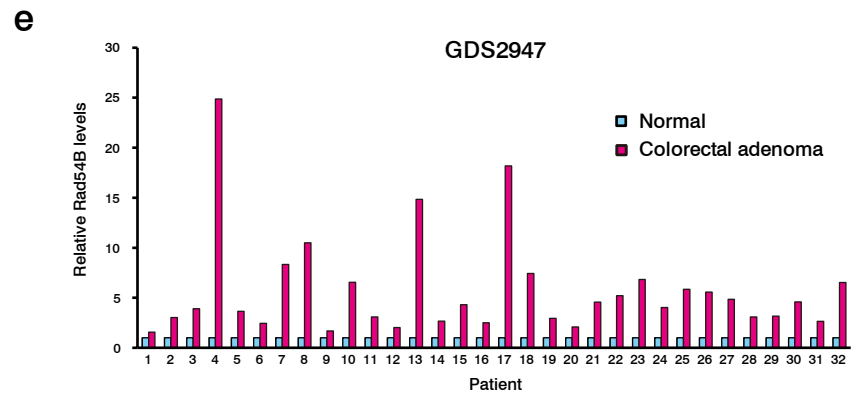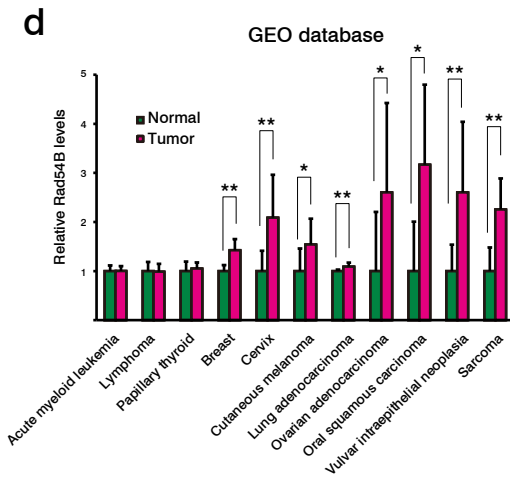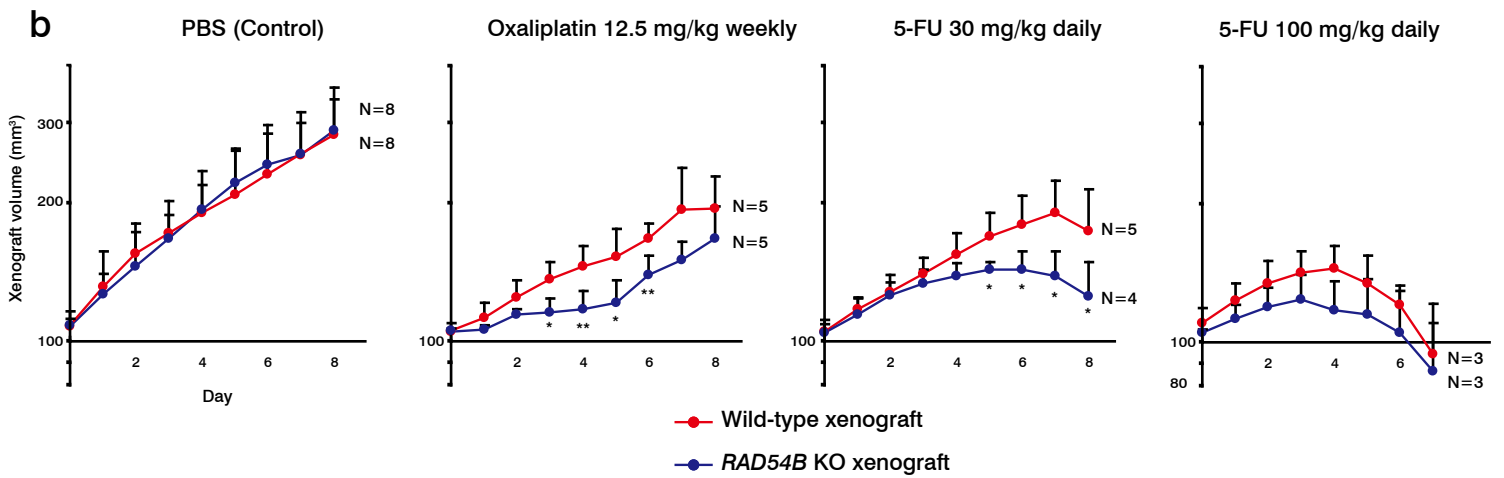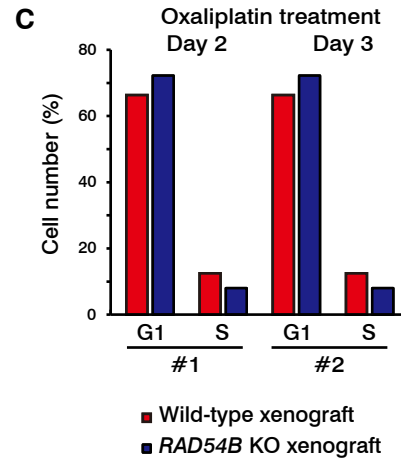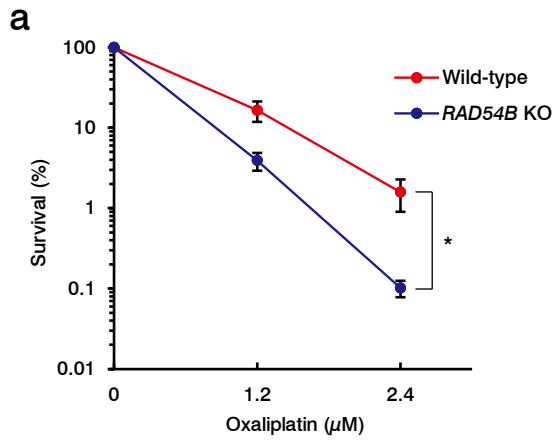
Figure-7 (Miyagawa)
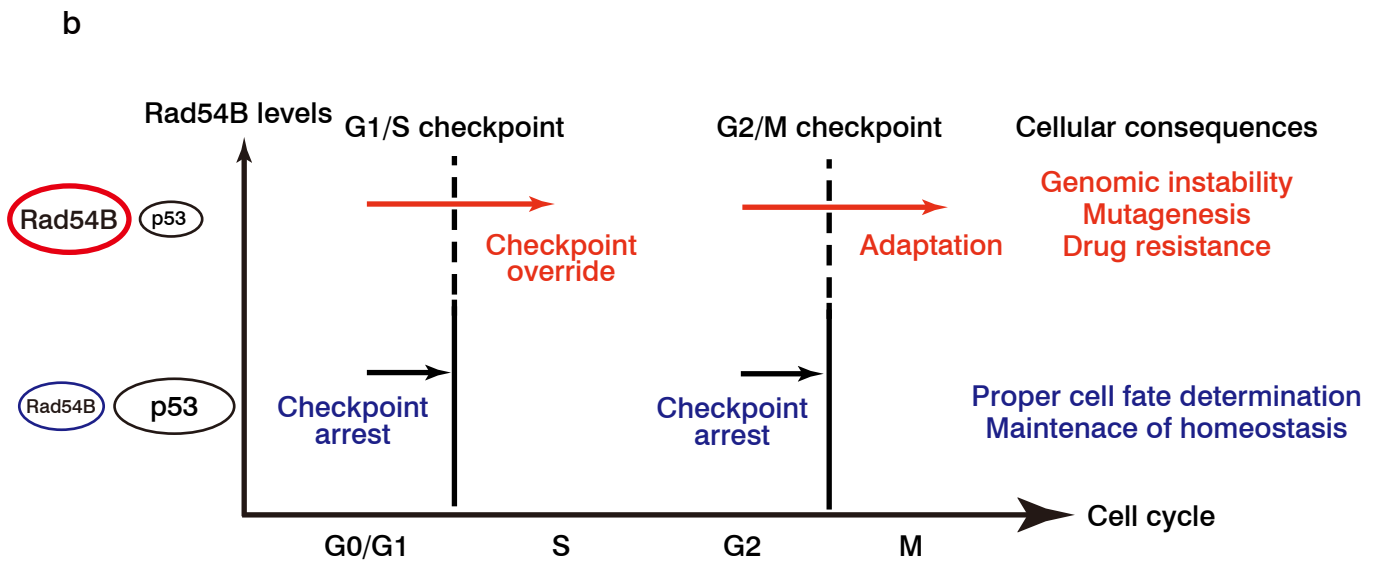
Supplementary Figure 1 | Rad54B is a novel DNA damage-responsive protein.
(**a**) The responses of Rad54B and p53 to IR in HCT116 cells. (**b**) The involvement of p21 in p53-mediated Rad54B repression was analyzed by RT-PCR (mean ± s.d.). n.s., not significant; * *P*<0.05, two-tailed *t*-test, n=3. (**c,d**) The responses of Rad54B upon DNA damage in H1299 cells (mean ± s.d.; n=3). (**e,f**) The levels of Rad54B mRNA after oxaliplatin treatment with or without ATM inhibition in HT-29 cells (mean ± s.d.; n=3). (**g**) The effects of Rad54B or MDM2 knockdown on the p53 levels. (**h**) The expression of p53 target genes in the steady state in Rad54B-knockdown cells (mean ± s.e.m.; n=4).
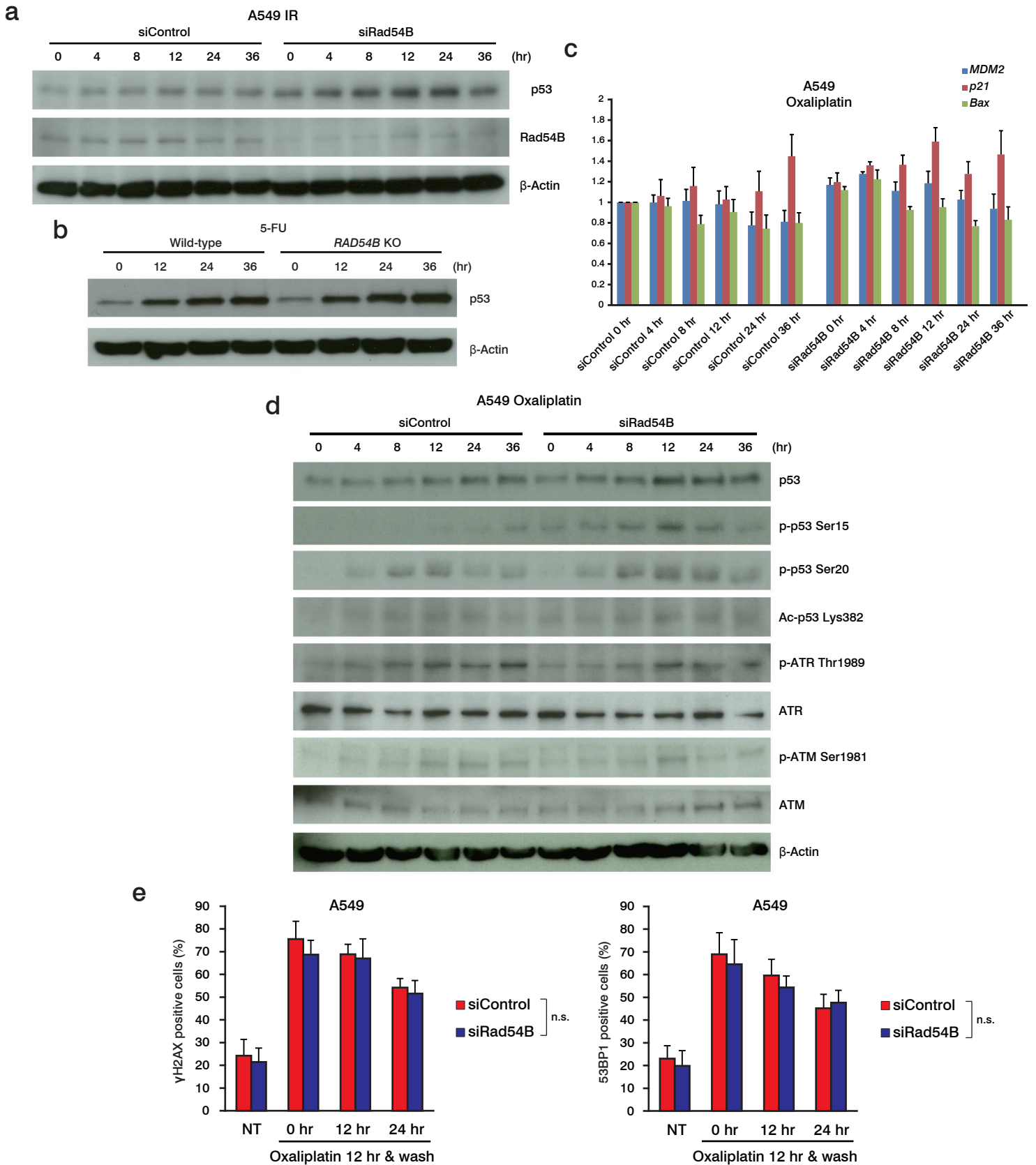
Supplementary Figure 2 | Rad54B downregulates the p53 levels and functions after DNA damage.
(**a,b**) Western blots for p53 after genotoxic stresses with Rad54B inhibition. (**c**) The expression of p53 target genes in Rad54B-knockdown cells after oxaliplatin treatment (mean ± s.d.; n=3). (**d**) The levels of p53, ATM, and ATR with modification upon oxaliplatin treatment were analyzed at the indicated time points by Western blot. (**e**) The number of γH2AX and 53BP1 foci-positive A549 cells at the indicated time points after oxaliplatin treatment and wash was counted (mean ± s.d.). n.s., not significant, two-tailed Welch's *t*-test, n=5 for each time point.
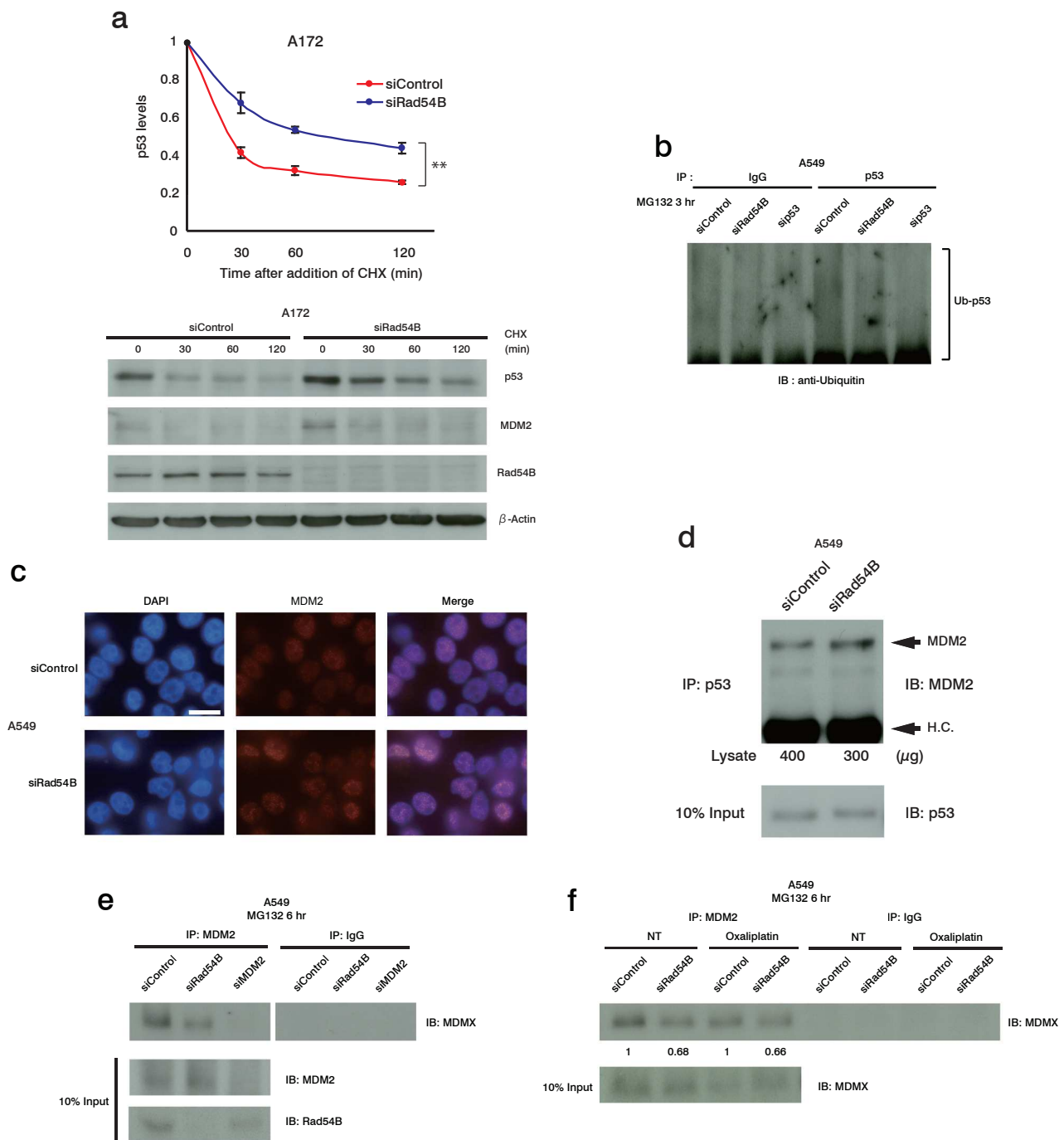
Supplementary Figure 3 | Rad54B reduces the stability of p53 by enhancing MDM2-MDMX heterodimerization.

(**a**) The effects of Rad54B on p53 stability in A172 cells (mean ± s.e.m.; n=3). ** P=0.0039, Wilcoxon matched-pairs signed-rank test. (**b**) p53 ubiquitination after proteasome inhibition was analyzed in parallel with p53 knockdown. Notably, the ubiquitinated materials observed here are derived from p53. (**c**) Rad54B-knockdown A549 cells were fixed and stained with an antibody against MDM2 (Red) and with DAPI (DNA; blue). Scale bar, 10 μm. (**d**) The MDM2-p53 interaction was analyzed by immunoprecipitation with an antibody against p53. To adjust the p53 levels in the lysate, the indicated amount of lysate from Rad54B-knockdown A549 cells was used. The Western blot shown below displays the same amount of p53 in the 10% input sample. (**e,f**) The MDM2-MDMX complex formation following MDM2 knockdown (**e**) or with DNA damage (**f**) was analyzed by immunoprecipitation after 6 hours of proteasome inhibition. The relative MDMX levels in the immunoprecipitate normalized to the input levels are shown.
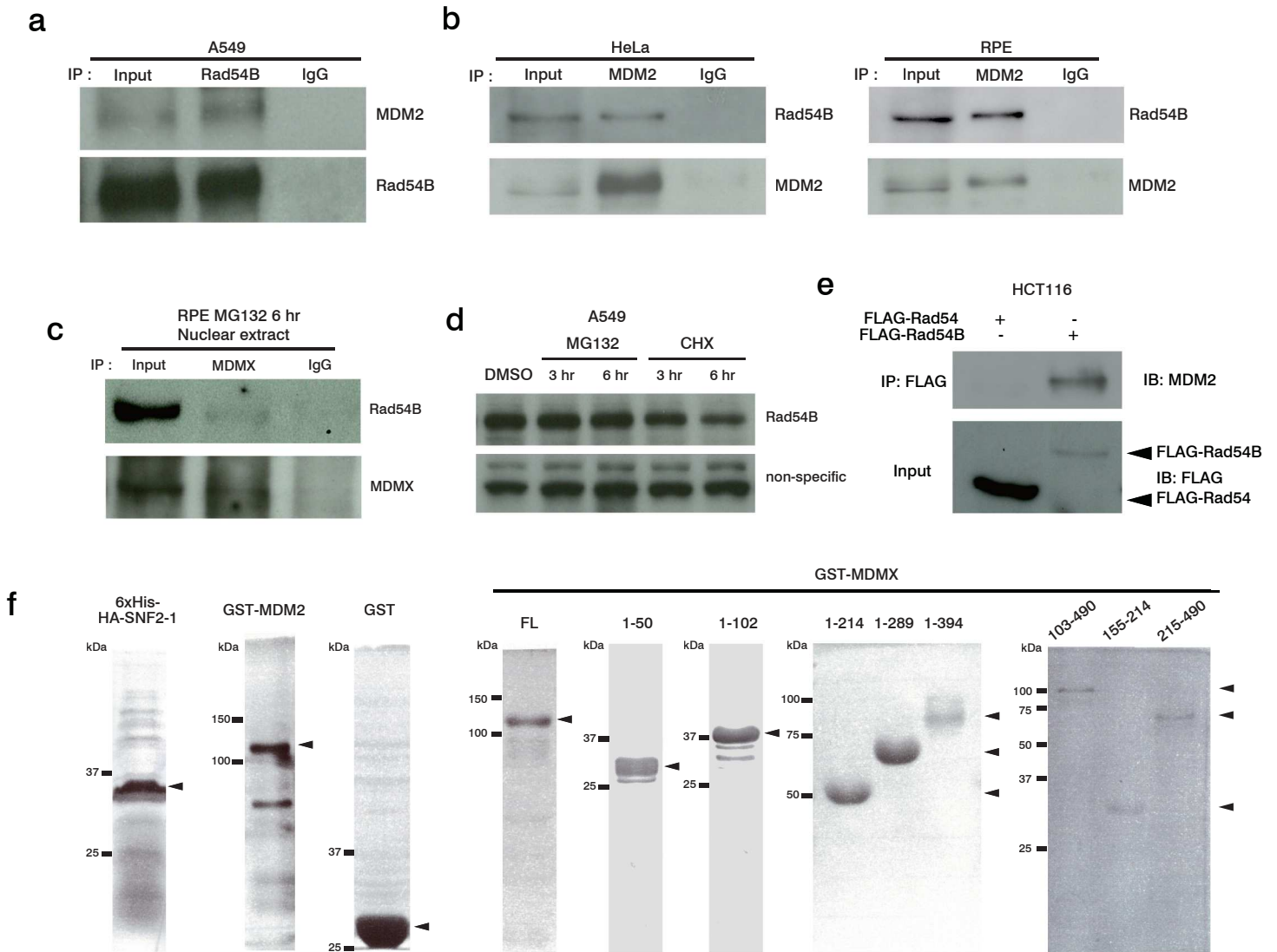
Supplementary Figure 4 | Rad54B interacts with MDM2 and MDMX.
(**a,b**) The interaction between endogenous Rad54B and MDM2 was detected by immunoprecipitation. (**c**) The interaction between endogenous Rad54B and MDMX was detected in the nuclear extract after proteasome inhibition. (**d**) The Rad54B levels after proteasome inhibition and protein synthesis inhibition were analyzed by Western blot. (**e**) The interaction between Rad54 and MDM2 was not detected in HCT116 cells. (**f**) The purity of the recombinant proteins used in this study was confirmed by Coomassie staining.
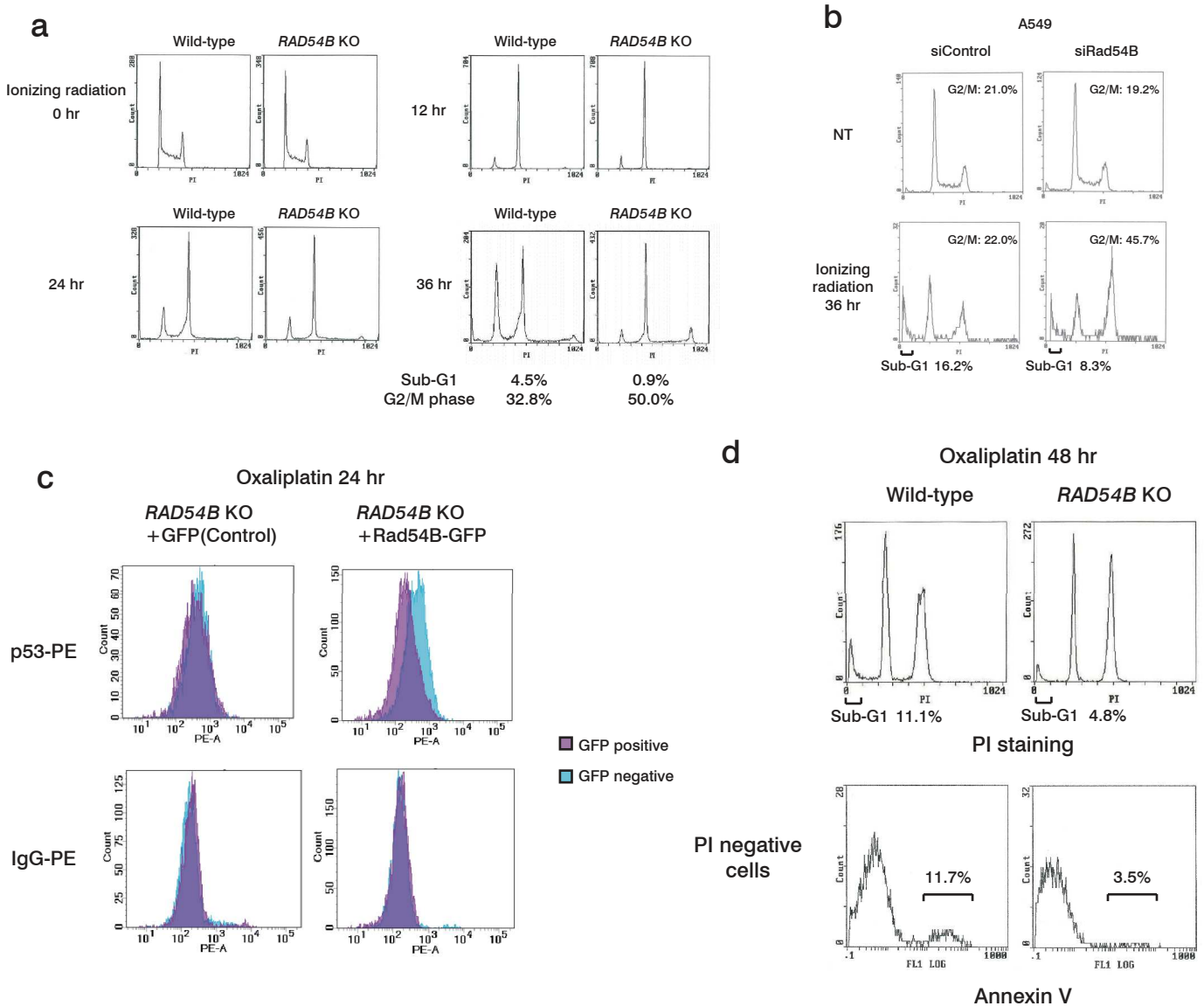
Supplementary Figure 5 | The Rad54B-p53 axis is involved in G2/M checkpoint maintenance.
(**a,b**) The number of G2/M-phase and sub-G1 *RAD54B* KO (**a**) or Rad54B-knockdown A549 (**b**) cells after IR was measured. The results are representative of more than three independent experiments. (**c**) The p53 levels in the Rad54B-complemented *RAD54B* KO cells after oxaliplatin treatment were analyzed by flow cytometry. The results are representative of three independent experiments. (**d**) Half of the cells treated with oxaliplatin were stained with propidium iodide (PI), while the other half were not permeabilized and were stained with an antibody against Annexin-V and with PI. The results are representative of three independent experiments.
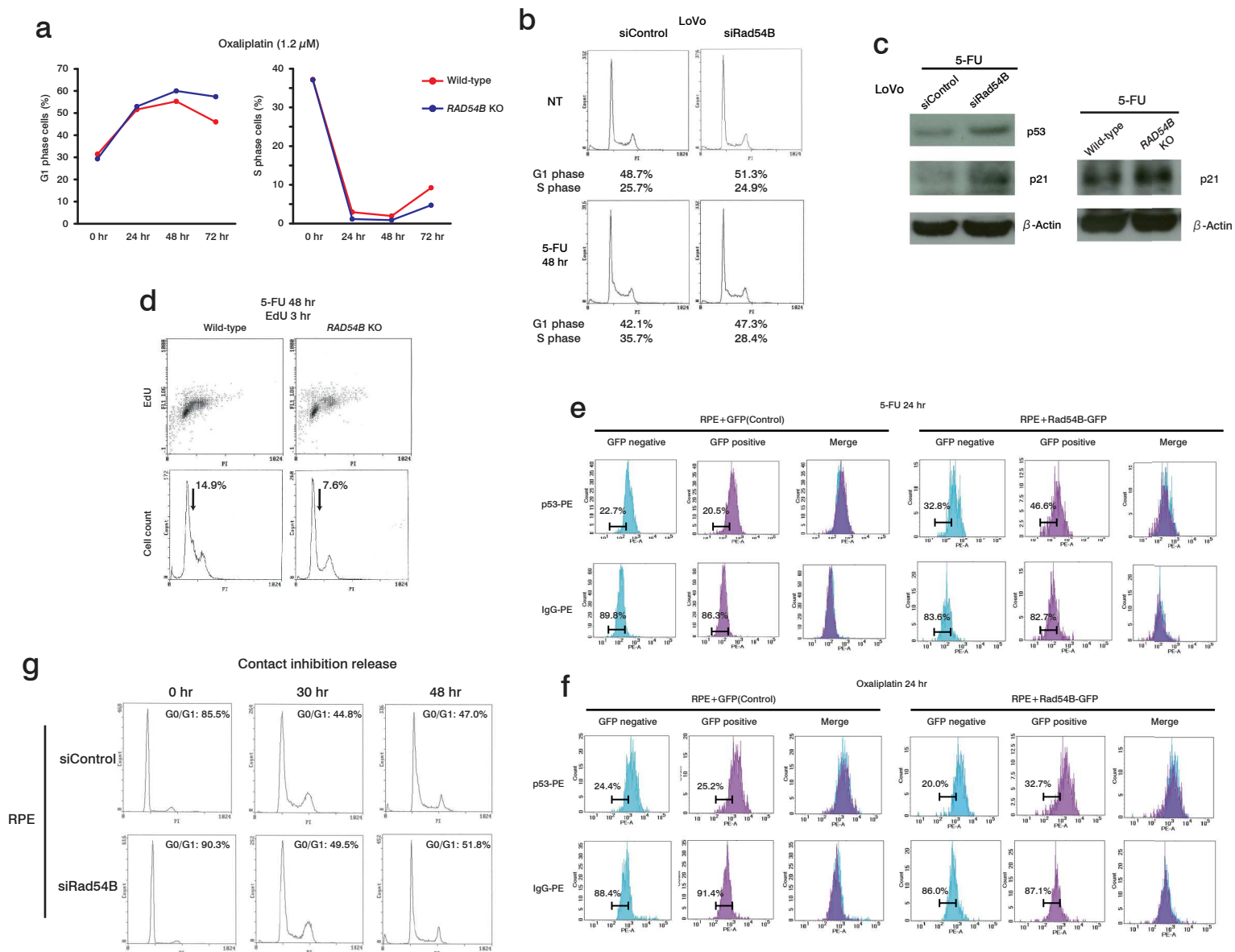
Supplementary Figure 6 | Rad54B is involved in G1/S checkpoint maintenance.
(**a**) The number of G1-phase and S-phase cells after oxaliplatin treatment was measured at the indicated time points. The results are representative of three independent experiments. (**b**) The number of S-phase cells after 5-FU treatment was measured in Rad54B-knockdown LoVo cells. The results are representative of three independent experiments. (**c**) The p21 levels after 5-FU treatment were analyzed in both Rad54B-knockdown LoVo cells and *RAD54B* KO cells. (**d**) The diagrams for EdU-incorporated S-phase cells after 5-FU treatment (upper panel) and the cell cycle distributions of whole cells (lower panel) are shown. The arrows indicate the early S-phase cells. The results are representative of three independent experiments. (**e,f**) The p53 levels in the Rad54B-overexpressing RPE cells after 5-FU (**e**) or oxaliplatin (**f**) treatment were analyzed by flow cytometry. The results are representative of more than three independent experiments. (**g**) The cell cycle progression of RPE cells after release from contact inhibition was analyzed. The results are representative of three independent experiments.
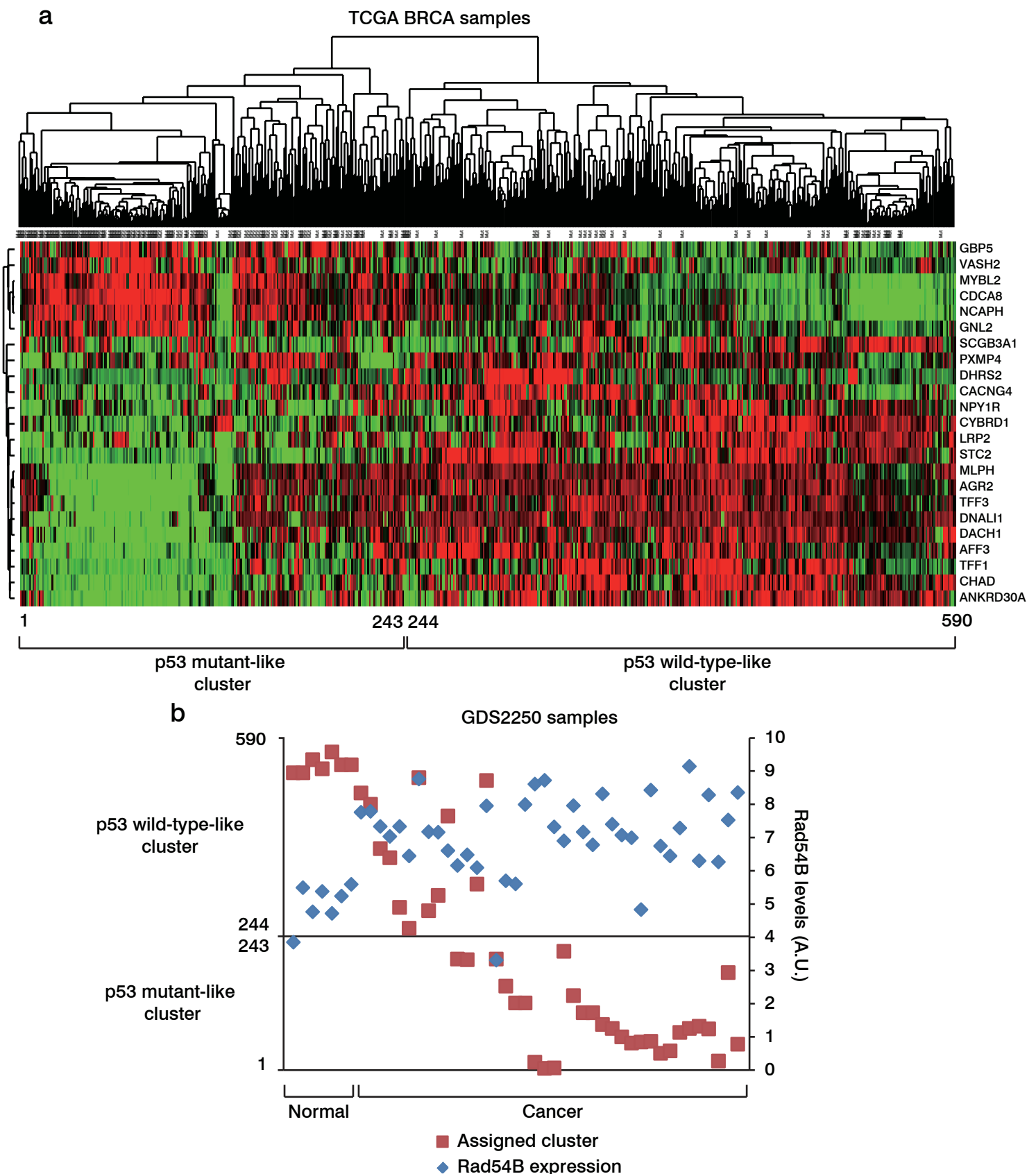
Supplementary Figure 7 | Prediction of the p53 mutation status of the breast cancer samples based on the gene expression patterns.

(**a**) TCGA BRCA samples were clustered according to the expression pattern of the p53 signature genes described in a previous study[23]. (**b**) GDS2250 samples were assigned to the cluster defined in (**a**) according to Pearson correlation-based similarity. Notably, Rad54B expression was higher in cancer samples than in normal samples, regardless of the predicted p53 status. See also Supplementary Table 2.
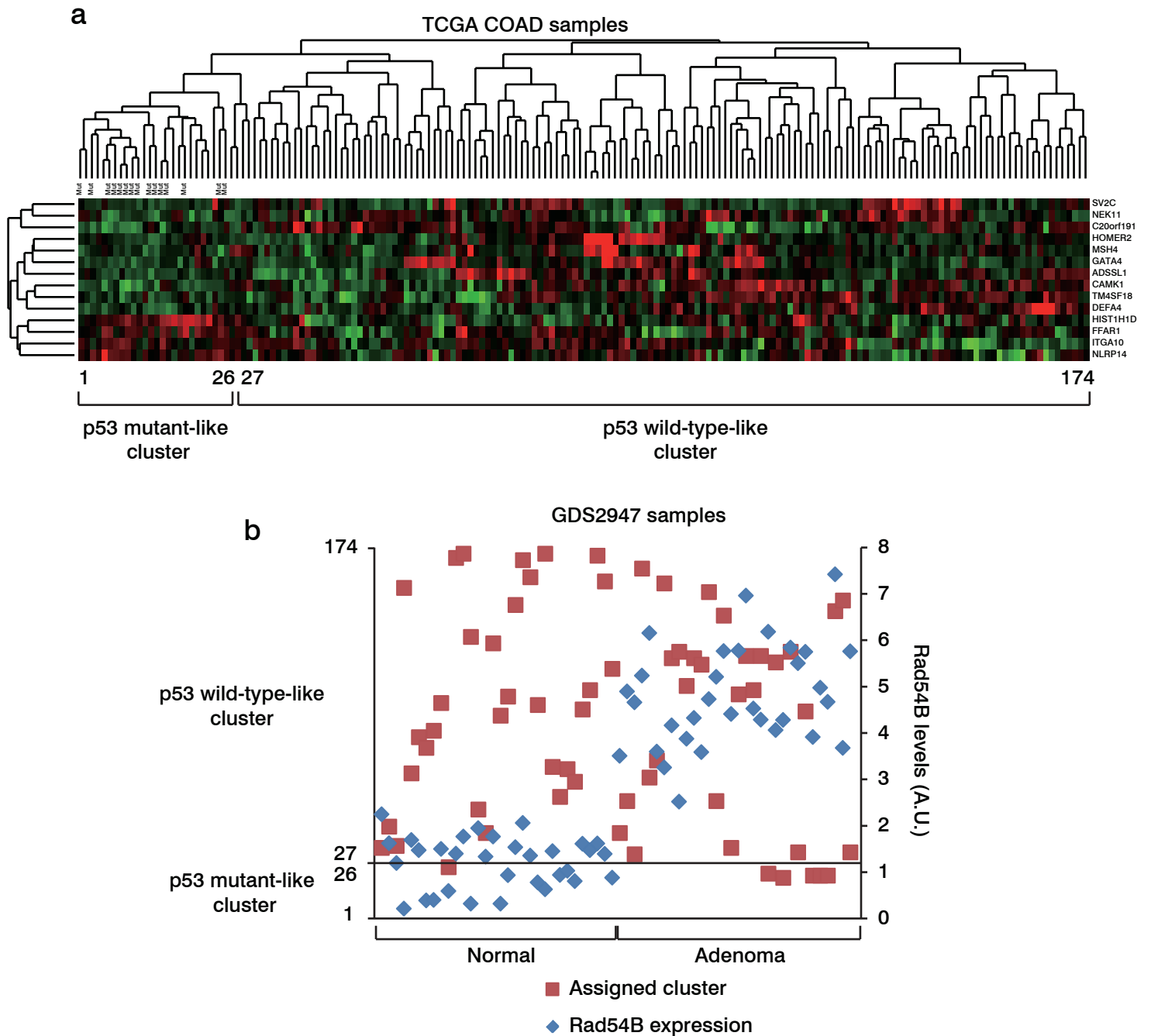
Supplementary Figure 8 | Prediction of the p53 mutation status of the colon adenoma samples based on the gene expression patterns.

(**a**) TCGA COAD samples were clustered according to the expression patterns of the gene set identified using the algorithm described in the Methods section. (**b**) GDS2947 samples were assigned to the cluster defined in (**a**) according to Pearson correlation-based similarity. Notably, Rad54B expression was higher in adenoma samples than in normal samples, regardless of the predicted p53 status. See also Supplementary Table 3.

a TCGA GBM samples

1   186   311   595

p53 mutant-like cluster   p53 wild-type-like cluster

b REMBRANDT samples

Rad54B low   Rad54B high

■ Assigned cluster
◆ Rad54B expression

Supplementary Figure 9 | Prediction of the p53 mutation status of the glioblastoma samples based on the gene expression patterns.

(**a**) TCGA GBM samples were clustered according to the expression patterns of the gene set identified using the algorithm described in the Methods section. (**b**) REMBRANDT samples were assigned to the cluster defined in (**a**) according to Pearson correlation-based similarity. Notably, the predicted frequency of the samples carrying a p53 mutation was not different between the groups of samples expressing high and low levels of Rad54B. See also Supplementary Table 4.

p53 functions	Range	Molecular state/treatment	Cellular level outcome	Clinical/in vivo outcome
	Toxic	*MDM2* KO *MDMX* KO	Extensive apoptosis and cell cycle arrest	Lethality
		Nutlin-3	Increase in apoptosis	Anti-tumor effects with adverse effects
	Effective	*RAD54B* KO/KD	Suppression of checkpoint escape	Suppression of drug resistance
		Normal		
	Mutagenic	Rad54B overexpression	Increase in adaptation (checkpoint escape)	Mutagenesis/drug resistance
		MDM2 overexpression	Decrease in apoptosis	Malignant conversion and progression
	Oncogenic	Mutation in p53	Defects in DDR, abberant proliferation	

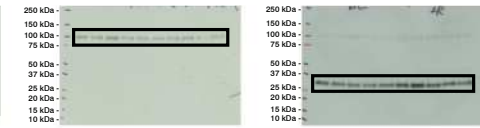**Supplementary Figure 10 |** The outcomes of changes in the p53 levels.
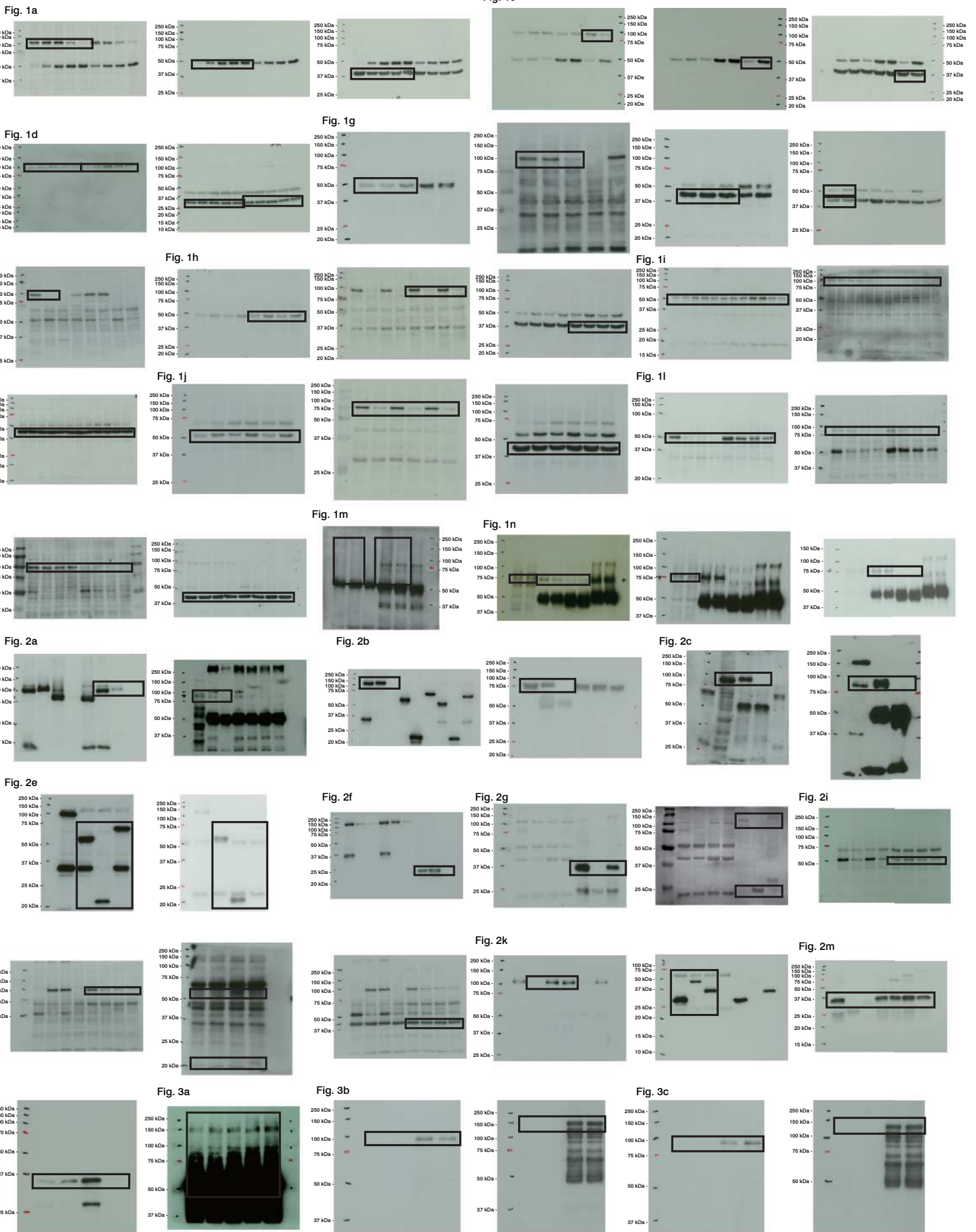
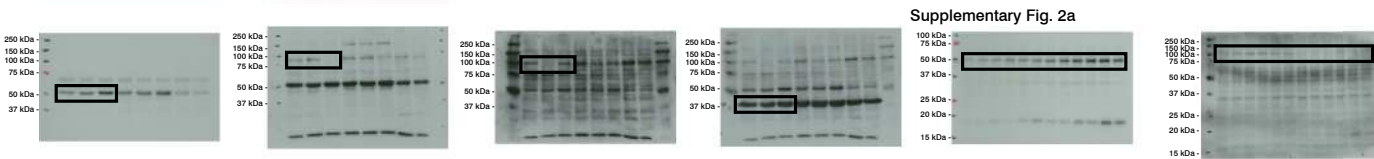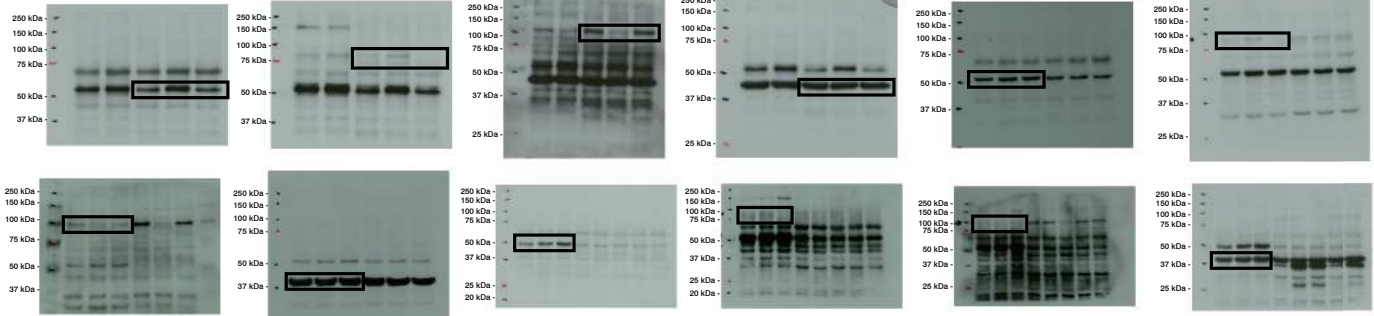**Supplementary Figure 11 |** Full scans of the blots in Figs. 1-3.

Supplementary Figure 12 | Full scans of the blots in Supplementary Figs. 1-4,6.
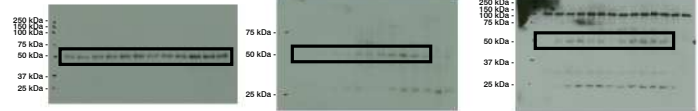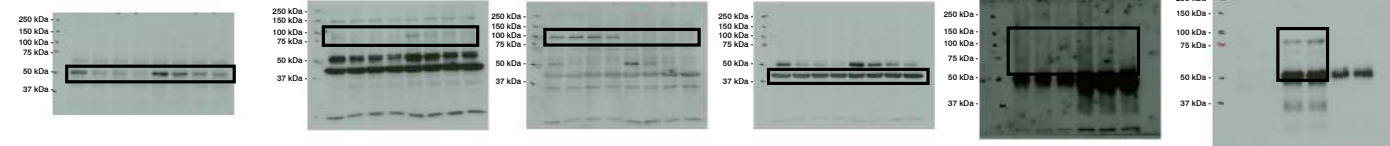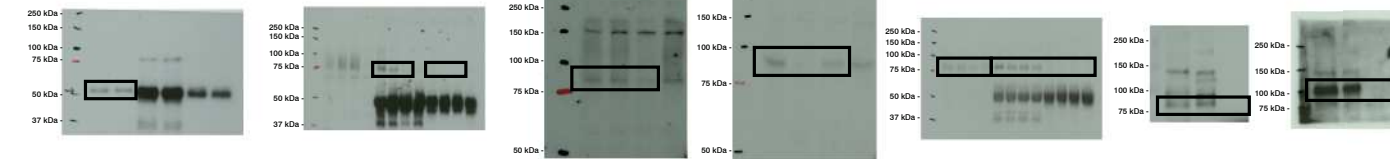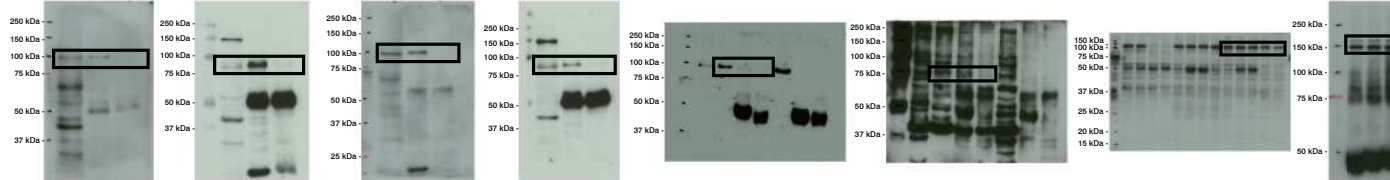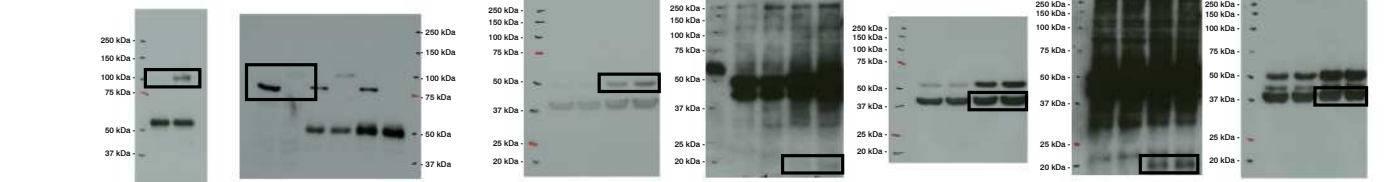
Supplementary Table 1 | Comparison of the Rad54B expression levels between the normal and neoplastic samples from the GEO database.

Organ, type	Sample number		Relative Rad54B levels		Mann-Whitney U-test	NCBI Accession Number
	normal	tumor	normal	tumor	P value	
Acute myeloid leukemia	38	26	1±0.12	1.00±0.10	0.309	GDS3057
Lymphoma	20	42	1±0.16	0.99±0.16	0.982	GDS3516
Papillary thyroid	7	7	1±0.19	1.05±0.12	0.798	GDS1732
Breast	7	40	1±0.12	**1.43±0.23	0.0001	GDS2250
Cervix	24	28	1±0.41	**2.09±0.87	<0.0001	GDS3233
Cutaneous melanoma	7	45	1±0.46	*1.54±0.52	0.0147	GDS1375
Lung adenocarcinoma	49	58	1±0.03	**1.09±0.08	<0.0001	GDS3257
Ovarian adenocarcinoma	12	12	1±1.21	*2.60±1.82	0.0141	GDS3592
Oral squamous carcinoma	4	16	1±1.01	*3.17±1.63	0.0160	GDS1584
Sarcoma	15	39	1±0.54	**2.60±1.44	<0.0001	GDS1209
Vulvar intraepithelial neoplasia	9	9	1±0.48	**2.26±0.63	0.0011	GDS2418

Organ, type	Patient number	Relative Rad54B levels		Rad54B levels		Tumor displaying elevated Rad54B expression	NCBI Accession Number
		normal (N)	tumor (T)	T > N	T ≤ N		
Colorectal adenoma	32	1±0.46	3.97±0.92	32	0	100%	GDS2947
Lung squamous carcinoma	5	1±0.02	1.08±0.06	4	1	80%	GDS1312

mean ± s.d., * P<0.05, ** P<0.01, Mann-Whitney U-test.

Supplementary Table 2 | Prediction of the p53 mutation status of the GDS2250 samples.

Database	Cluster	p53-mutated samples in each cluster	Risk of p53 mutation[a]	
TCGA BRCA (N=590)	1-243	139	57.2%	
	244-590	27	7.8%	
Database Group	Cluster	Number of samples in each cluster[b] (% total)	Predicted number of p53-mutated samples for each cluster[*]	Predicted number of p53-mutated samples for group (% total)
GDS2250 Normal (N=7)	1-243	0 (0%)	0	0.5 (7.8%)
	244-590	7 (100%)	0.5	
GDS2250 Cancer (N=40)	1-243	28 (70%)	16	17.0 (42.3%)
	244-590	12 (30%)	0.9	

* calculated as (a) × (b).

Supplementary Table 3 | Prediction of the p53 mutation status of the GDS2947 samples.

Database	Cluster	p53-mutated samples in each cluster	Risk of p53 mutation[a]	
TCGA COAD (N=174)	1-26	15	57.7%	
	27-174	0	0%	
Database Group	Cluster	Number of samples in each cluster[b] (% total)	Predicted number of p53-mutated samples for each cluster[*]	Predicted number of p53-mutated samples for group (% total)
GDS2947 Normal (N=32)	1-26	1 (3.1%)	0.6	0.6 (1.8%)
	27-174	31 (96.9%)	0	
GDS2947 Adenoma (N=32)	1-26	5 (16%)	2.9	2.9 (9.0%)
	27-174	27 (84%)	0	

* calculated as (a) × (b).

Supplementary Table 4 | Prediction of the frequency of the REMBRANDT samples carrying a p53 mutation.

Database	Cluster	p53-mutated samples in each cluster	Risk of p53 mutation[a]	
	1-186	49	26.3%	
TCGA GBM (N=595)	187-310	19	15.3%	
	311-595	15	5.3%	
Database Group	Cluster	Number of samples in each cluster[b] (% total)	Predicted number of p53-mutated samples for each cluster[*]	Predicted number of p53-mutated samples for group (% total)
	1-186	56 (41.5%)	14.8	
REMBRANDT Rad54B low (N=135)	187-310	15 (11.1%)	2.3	20.4 (15.1%)
	311-595	64 (47.4%)	3.4	
	1-186	97 (43.5%)	25.6	
REMBRANDT Rad54B high (N=223)	187-310	18 (8.1%)	2.8	34.0 (15.2%)
	311-595	108 (48.4%)	5.7	

* calculated as (a) × (b).

Supplementary Table 5 | Antibodies used in this study.

Source/reference	Antibody	Dilution
Ref. 10	Rabbit polyclonal anti-Rad54B	1:500 for Western blot
Bethyl Laboratories, Inc.	Goat polyclonal anti-MDMX (A303-870A)	1:500 for Western blot
Cell Signaling Technology	Acetyl-p53 (Lys382) (#2525)	1:500 for Western blot
	Phospho-ATM (Ser1981) (#4526)	1:500 for Western blot
	Phospho-p53 (Ser15) (#9284)	1:500 for Western blot
	Phospho-p53 (Ser20) (#9287)	1:500 for Western blot
GeneTex	ATR (phospho Thr1989) (GTX128145)	1:500 for Western blot
Jackson ImmunoResearch	R-phycoerythrin-conjugated anti-mouse IgG (115-116-146)	1:100 for flow cytometry
MBL	Multi Ubiquitin FK2 (D058-3)	1:500 for Western blot
	Annexin V-FITC (4700-100)	1:10 for flow cytometry
Millipore	MDM2 2A10 (OP115)	1:500 for Western blot
	MDMX 8C6 (#04-1555)	1:500 for Western blot
	p53 Binding Protein 1 (PC712)	1:500 for immunofluorescence
	Phospho-Histone H2A.X (Ser139) (#05-636)	1:500 for immunofluorescence
	Phospho-Histone H3 (Ser 10) (#06-570)	1:500 for immunofluorescence
Novus Biologicals	Rabbit polyclonal anti-ATM (NB100-104)	1:500 for Western blot
Santa Cruz Biotechnology	ATR N-19 (sc-1887)	1:500 for Western blot
	Cdk2 M2 (sc-163)	1:1,000 for Western blot
	MDM2 SMP14 (sc-965)	1:200 for Western blot
		2µg for immunoprecipitation
		1:200 for immunofluorescence
	p21 187 (sc-817)	1:200 for Western blot
	p53 DO-1 (sc-126)	1:1,000 for Western blot
		1µg for immunoprecipitation
		1:100 for flow cytometry
	Rad54B 19-K2 (sc-101234)	1:100 for Western blot
		1µg for immunoprecipitation
Sigma Aldrich	β-Actin AC-15 (A5441)	1:10,000 for Western blot
	FLAG M2 (F3165, F1804)	1:1,000 for Western blot (F3165)
		1µg for immunoprecipitation (F1804)
	HA-7 (H6533, H9658)	1:1,000 for Western blot (H6533)
		1µg for immunoprecipitation (H9658)